SEMMELWEIS EGYETEM

DOKTORI ISKOLA

Ph.D. értekezések

3450.

CZIGLÉCZKI JANKA ZSÓFIA

A gyógyszerészeti tudományok korszerű kutatási irányai

című program

Programvezető: Dr. Antal István, egyetemi tanár

Témavezető: Dr. Balog Erika, habilitált egyetemi docens

INVESTIGATION OF THE FUNCTIONAL MECHANISM OF SMALL G PROTEIN RAN

PhD thesis

Janka Zsófia Czigléczki

Semmelweis University Doctoral College

Pharmaceutical Sciences and Health Technologies Division

Supervisor: Erika Balog, PhD

Official reviewers: András Czajlik, PhD
Dóra K. Menyhárd, PhD

Head of the Complex Examination Committee: Prof. Romána Zelkó, DSc, PhD

Members of the Complex Examination Committee: Balázs Balogh, PhD
Dóra K. Menyhárd, PhD

Budapest
2026

TABLE OF CONTENTS

List of Abbreviations

aMDeNM	Adaptive Molecular Dynamics with excited Normal Modes
CRM1	Chromosomal Region Maintenance 1
GAP	GTPase-activating protein
GDI	Guanine nucleotide dissociation inhibitor
GDP	Guanosine diphosphate
GEF	Guanine nucleotide exchange factor
GNRP	Guanine nucleotide-releasing protein
GTP	Guanosine triphosphate
HEAT	Huntingtin, Elongation factor 3 (EF3), Protein phosphatase 2A (PP2A), Target of Rapamycin 1 (TOR1)
MD	Molecular Dynamics
MDeNM	Molecular Dynamics with excited Normal Modes
NES	Nuclear export signal
NLS	Nuclear localization signal
NM	Normal Mode
NPC	Nuclear pore complex
NTF2	Nuclear Transport Factor 2
NTR	Nuclear transport receptor
PDB	Protein Data Bank
P-loop	phosphate-binding loop
Ran	Ras-related Nuclear protein
RanBPs	Ran-binding proteins
RCC1	Regulator of Chromosome Condensation 1
RMSD	Root-mean square deviation
RMSF	Root-mean square fluctuation
SAF	Spindle Assembly Factor

1. INTRODUCTION

1.1. Scientific background

1.1.1. Motivation for the research

The small GTPase Ran (**Ra**s-related **N**uclear protein) is a central regulator of cellular organization, coordinating mitotic spindle formation through the release of microtubule-stabilizing factors from importin-mediated inhibition, post-mitotic nuclear envelope assembly via membrane fusion and nuclear pore formation, and nucleo-cytoplasmic transport by acting as a positional cue that governs the assembly and disassembly of import and export complexes. Disruption of Ran signaling leads to severe mitotic abnormalities, including spindle disorganization and chromosomal instability (1).

Recent studies have shown that Ran is differentially overexpressed in various human cancers (2), while its loss is well tolerated in normal cells without compromising viability or mitotic function. This suggests that tumor cells acquire a dependency on Ran signaling for proliferation and survival, highlighting Ran as a potential selective therapeutic target. Moreover, Ran hyperactivation has been linked to cellular transformation, tumor progression, and metastasis in multiple cancer types (3), notably in breast cancer, where inhibition of Ran activation induces preferential cytotoxicity in malignant cells (4). The functional roles of Ran are intricately connected to its interactions with importins, exportins, and Ran-binding proteins (RanBP1 and RanBP2), emphasizing its centrality in nuclear transport and mitotic regulation (5).

Given its consistent overexpression in tumors, along with its prognostic significance and therapeutic potential, further investigation into the mechanisms regulating Ran function is essential. However, experimental studies on Ran remain somewhat constrained by limitations in structural biology techniques, which can make it challenging to fully characterize its conformational dynamics and molecular interactions in detail. To overcome these limitations, computational simulation approaches provide a valuable alternative for investigating the structure and behavior of the small GTPase Ran under various conditions. Therefore, the aim of this study is to explore the structural features and dynamic properties of Ran using simulation-based methods.

1.1.2. The Ras superfamily of small GTPases

In general, the Ras GTPase superfamily (6), to which Ran belongs, comprises low-molecular-weight (20-30 kDa), monomeric GTP-binding proteins that function as molecular switches, cycling between inactive GDP-bound and active GTP-bound states (7, 8). These proteins transduce extracellular and intracellular signals to regulate essential cellular processes, including proliferation, differentiation, adhesion, migration, polarity, survival, and apoptosis (9, 10). Dysregulation of Ras GTPase signaling leads to numerous human diseases, including cancer, neurodegenerative disorders, and cardiovascular conditions (11, 12). Ras proteins are localized to specific membrane microdomains or cytoplasmic compartments. In the active form, Ras proteins bind selective effector molecules, initiating downstream signaling cascades that control transcription, cytoskeletal dynamics, and vesicular trafficking.

Structural Organization

Ras superfamily members share a conserved GTP-binding domain (G-domain) and a short C-terminal segment known as the hypervariable region (HVR), which exhibits the greatest sequence diversity among these proteins.

The G-domain contains characteristic motifs (G1-G5) involved in nucleotide binding and hydrolysis (6, 13, 14)(Figure 1):

- G1 (P-loop, GxxxxGKS/T): binds phosphate groups of GDP/GTP.
- G2 (switch I, invariant residue T): undergoes conformational changes to form part of the effector-binding surface.
- G3 (switch II, DxxGQ/H/T): coordinates Mg^{2+} ions for catalysis.
- G4 (N/TK/QxD): ensures guanine nucleotide specificity.
- G5 (C/S/T/ASA/K/L): stabilizes nucleotide binding through interactions with G4.

The hypervariable region (HVR) dynamically interacts with the catalytic domain and contributes to protein-specific functions. Notably, it plays a central role in membrane

association, primarily through post-translational modifications (such as farnesylation, prenylation and palmitoylation) and interactions with lipid membranes (15, 16).

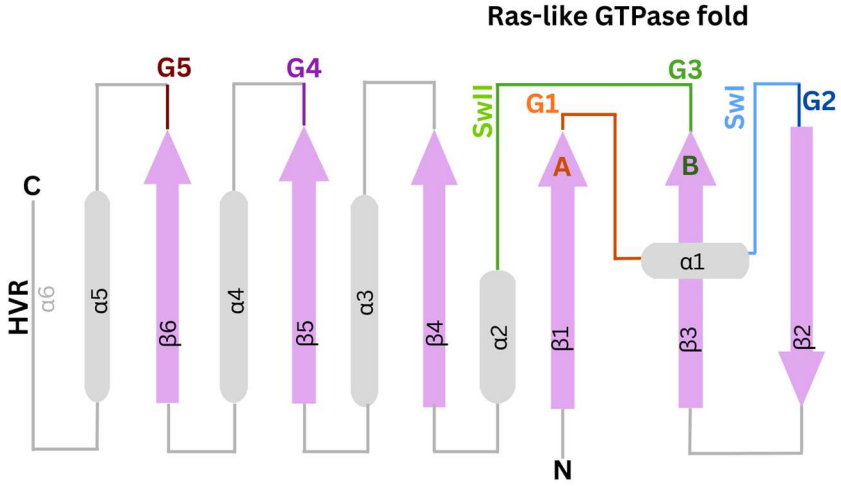

Figure 1. Topology of small Ras-like GTPases. *β-strands (pink) and α-helices (gray) are labeled. G1 (orange), G2 (dark blue), G3 (dark green), G4 (purple), G5 (dark red), switch I (SwI; light blue), and switch II (SwII; light green) motifs are highlighted in the topology diagram. (17)*

GDP- and GTP-bound states share a conserved α/β fold, but conformational changes in switch I and switch II allow selective effector binding. Functional diversity arises from minor sequence variations, structural differences, and post-translational modifications such as farnesylation or palmitoylation, which determine subcellular localization and specific interactions with regulators and effectors (18, 19).

Regulation

Ras superfamily members act as binary switches, alternating between inactive GDP-bound and active GTP-bound states. Their low intrinsic nucleotide exchange and GTP hydrolysis rates require regulatory proteins (20-24):

- GEFs: guanine nucleotide exchange factors; catalyze GDP release and GTP binding, activating the GTPase.
- GAPs: GTPase-activating proteins; accelerate GTP hydrolysis, returning the GTPase to its inactive state.
- GNRPs (guanine nucleotide-releasing proteins): facilitate GDP release and GTP rebinding for some GTPases.
- GDIs (guanine nucleotide dissociation inhibitors): sequester some GTPases in the cytosol, preventing membrane association and effector interaction.

Upstream stimuli, such as growth factors, hormones, and extracellular matrix signals, regulate these factors, allowing Ras GTPases to integrate multiple inputs. Transition between GDP- and GTP-bound states induces conformational changes that increase effector affinity, triggering downstream signaling pathways until GTP hydrolysis restores the inactive state (11, 18, 25).

Subgrouping and Functional Diversity

Despite a conserved GTP-binding fold, Ras superfamily members exhibit significant functional diversity. Phylogenetic and biochemical analyses classify the superfamily into five major families: Ras, Rho, Rab, Arf, and Ran (6, 26, 27).

- Ras family: regulates proliferation, survival, and differentiation through MAPK and PI3K pathways.
- Rho family: controls cytoskeletal dynamics, polarity, and motility.
- Rab family: mediates vesicular trafficking, membrane identity, and vesicle docking.
- Arf family: regulates vesicle formation, lipid metabolism, and Golgi organization.
- Ran family: primarily mediates nucleocytoplasmic transport and mitotic spindle assembly.

Members within each family are further diversified by membrane-targeting motifs and post-translational modifications, which determine subcellular localization and dynamic regulation. Cross-talk among families coordinates complex cellular processes, emphasizing the Ras superfamily as a central hub in cellular signaling networks.

1.1.3. Overview of Ran functions

Nucleo-cytoplasmic transport

In eukaryotic cells, the nucleus serves as the central repository of genetic material, housing the cell's DNA and coordinating essential processes such as transcription, replication, and chromatin organization. However, the majority of metabolic and signaling activities that sustain cellular life take place in the cytoplasm. To maintain proper cellular function, it is therefore crucial that the nucleus and cytoplasm engage in continuous and highly regulated communication. The exchange is mediated by

specialized structures known as nuclear pore complexes (NPCs) (28, 29). NPCs are large, multi-protein assemblies embedded throughout the nuclear envelope that form selective transport channels, allowing bidirectional traffic between the nucleoplasm and the cytoplasm (30). Transport across the NPC occurs via two primary mechanisms: passive diffusion and facilitated transport. Small molecules and ions can freely diffuse through the NPC, whereas the movement of larger macromolecules is restricted by the selective permeability barrier formed by intrinsically disordered nucleoporins that line the pore (31, 32). To overcome this barrier, larger cargoes rely on facilitated transport mediated by nuclear transport receptors (NTRs), also known as karyopherins. These receptors specifically recognize nuclear localization signals (NLSs) or nuclear export signals (NESs) present on their cargo molecules, enabling selective import into or export out of the nucleus (33, 34).

Ran was first identified as a key factor involved in protein import into the nucleus and has since been recognized as an essential regulator of nucleocytoplasmic transport (5, 35-37). The directionality of this transport depends on a concentration gradient of Ran bound to GTP or GDP, with RanGTP being predominantly localized in the nucleus and RanGDP concentrated in the cytoplasm (38). As previously mentioned, similarly to other members of the Ras superfamily of small GTPases, Ran cycles between two conformations: a GTP-bound active form and a GDP-bound inactive form. This conformational switching determines its interaction with effector proteins, thereby directing cargo recognition, transport directionality, and timing of macromolecular trafficking across the nuclear envelope (39).

The asymmetric distribution of Ran is maintained by a coordinated network of Ran regulators. Nuclear RanGTP is sustained through the import of RanGDP by nuclear transport factor 2 (NTF2) (40), a cytosolic protein that interacts specifically with RanGDP (41, 42). The shuttling of NTF2 itself is a regulated process in mammalian cells, potentially influenced by tyrosine kinase-dependent signaling pathways. Within the nucleus, RCC1 (Regulator of Chromosome Condensation 1) (43) acts as the GEF for Ran (44), catalyzing the exchange of GDP for GTP (45). RCC1 is anchored to chromatin via nucleosomes, ensuring the localized generation of RanGTP near the chromosomes. Conversely, in the cytoplasm, RanGAP1 and RanBP1 stimulate the hydrolysis of RanGTP

to RanGDP, thereby reinforcing the RanGTP/RanGDP gradient that is essential for directionality (46-49).

RanGTP also drives the formation and disassembly of nuclear transport complexes. For example, importins (such as the importin-α/importin-β heterodimer) recognize cargo proteins containing classical NLSs in the cytoplasm, transport them into the nucleus, and release them upon interaction with RanGTP (50). The resulting RanGTP-importin-β complex is then recycled back to the cytoplasm for another round of transport. Structural analyses have shown that importin-β contains HEAT repeat motifs that can flexibly open or close to accommodate binding partners, with RanGTP stabilizing these conformational states (35, 51). Similarly, RanGTP regulates nuclear export by controlling the assembly of export complexes. In humans, at least eight RanGTP-dependent exportins have been identified, each recognizing distinct cargoes (34). For instance, exportin 6 selectively exports actin, preventing its nuclear accumulation, whereas CRM1 (exportin 1) transports a wide range of cargoes (52) and is inhibited by leptomycin B (53).

The nucleocytoplasmic transport machinery itself is also dynamically regulated. Several Ran regulators shuttle between the nucleus and cytoplasm—for example, RCC1 contains an NLS that facilitates its nuclear import via the importin-α/importin-β complex, whereas RanBP1 cycles between compartments but remains predominantly cytoplasmic, and RanGAP1 is excluded from the nucleus due to its NES (54, 55). Additionally, CAS (CSE1) mediates the export of importin-α to the cytoplasm, ensuring continuous transport activity. Collectively, these tightly coordinated processes maintain protein gradients across the nuclear envelope, ensuring proper spatial organization of Ran and its regulatory partners.

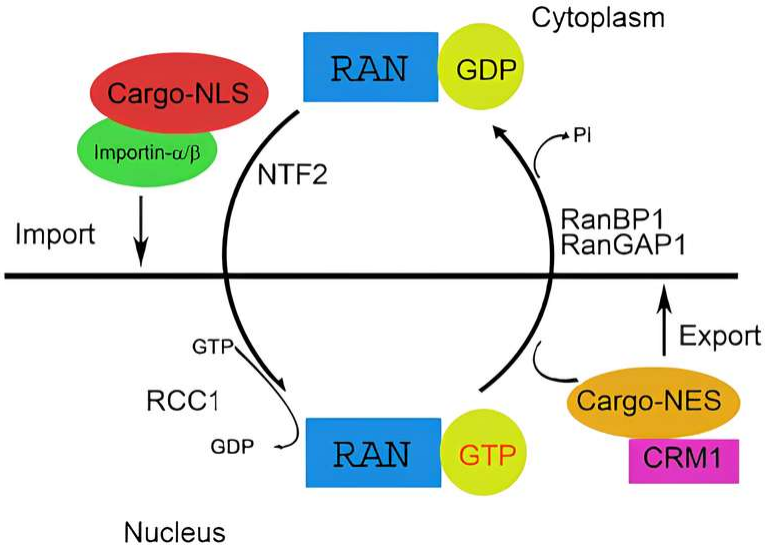

Figure 2.Ran-mediated nucleocytoplasmic transport of proteins. *High RanGTP concentration is maintained in the nucleus by nucleotide exchange with the aid of regulator of chromosome condensation (RCC1). Cargo containing a nuclear export signal (NES) can bind to RanGTP and be transported out of the nucleus. In the cytoplasm, RanBP1 forms a complex specifically with RanGTP and enhances RanGAP1-mediated hydrolysis of RanGTP to RanGDP. Subsequently, a conformational change in Ran leads to the dissociation of the export cargo from the complex, while RanGDP translocates back to the nucleus and waits for another round of nuclear export once it is converted to active RanGTP. The figure has been published by Doherty et al.* (56)

Mitotic spindle formation and nuclear envelope assembly

In addition to its essential function in nucleocytoplasmic transport, Ran also plays a distinct and critical role in cell cycle regulation (5). Early evidence for this role came from studies showing that a point mutation in RCC1, the guanine nucleotide exchange factor for Ran, caused premature chromosome condensation, linking Ran activity to proper cell cycle progression (43). Subsequent research across several organisms confirmed Ran's involvement in regulating the cell cycle (57). In human cells, the expression of a dominant-active Ran Q69L mutant disrupts normal progression, leading to cell cycle arrest, predominantly in the G_2 phase, and to a lesser extent, in the G_1 phase (3, 58-60). Similarly, disruption of the Ran system in yeast produces comparable defects, while mutations in the RCC1 homolog Dcd1/Pim1 cause defects at the end of mitosis - defects that can be rescued by the Ran homolog Spi1 (61).

Beyond its role in regulating cell cycle checkpoints, Ran is a key regulator of mitotic spindle assembly during mitosis (5, 62). The mitotic spindle, a dynamic

microtubule-based structure, ensures accurate segregation of replicated chromosomes into daughter cells (57). Multiple studies have demonstrated that RanGTP promotes spindle assembly. For instance, increasing the level of GTP-bound Ran—by adding either RCC1 or dominant-active Ran mutants—enhances spindle formation in Xenopus egg extracts, whereas inhibition of RanGTP formation causes abnormal spindle assembly (47). Similar mitotic defects have been observed in somatic cells when Ran activity is perturbed, emphasizing the conserved role of Ran in spindle organization. RanGTP facilitates microtubule nucleation and dynamics near chromosomes by releasing spindle assembly factors (SAFs) from inhibitory complexes with importins. During interphase, these SAFs contain NLSs and are bound by importin-α/importin-β dimers, keeping them inactive. During mitosis, RanGTP binds to importin-β, displacing the SAFs and releasing them to promote spindle assembly. In this manner, RanGTP repurposes components of the nucleocytoplasmic transport system to ensure that active SAFs are localized near chromatin, facilitating spindle formation and function.

Ran also plays an essential role in nuclear envelope reassembly at the completion of mitosis (63). The disassembly of the nuclear envelope during early mitosis is followed by its reformation around segregated chromatin in late mitosis and early interphase. Early studies demonstrated that mutations in RCC1 in Schizosaccharomyces pombe resulted in nuclear envelope fragmentation (61), mislocalization of pore-containing membranes, and uncompartmentalized chromatin, highlighting the importance of Ran in nuclear architecture. Experiments using Xenopus egg extracts and demembraned sperm chromatin (64) confirmed that Ran is required for nuclear membrane assembly (65) and lamina formation.

Further studies revealed that membrane vesicles, which fuse to form the nuclear envelope, accumulate around chromatin coated with recombinant Ran protein (66). These vesicles contain nucleoporins, form NPCs, and support active nuclear import within the resulting pseudo-nuclei. Inhibition of RCC1 or RanGAP1 reduces vesicle recruitment and fusion, indicating that both GTP loading and GTP hydrolysis by Ran are necessary for nuclear envelope formation (66). Specifically, RCC1-mediated generation of RanGTP is required for vesicle recruitment, while RanGTP hydrolysis facilitates vesicle fusion events.

Although the precise mechanisms underlying Ran's role in nuclear envelope formation remain not completely understood, importin-β appears to be an important mediator. RanGTP produced near chromosomes can release nucleoporins from inhibitory complexes with importin-β, thereby promoting pore complex assembly and membrane fusion (29). Together, these processes demonstrate that both the generation and hydrolysis of RanGTP are essential for the sequential steps of nuclear envelope reformation, highlighting Ran's central function in maintaining cellular organization and mitotic fidelity.

1.1.4. Structural characteristics of the small GTPase Ran

The first 3D structure of cytosolic Ran was determined using X-ray crystallography. Scheffzek et al. (67) reported the GDP-bound structure, which was compared with the RasGDP structure to describe its characteristic structural features. The tertiary structure of RanGDP, with highlighted secondary structures, is displayed in Figure 3.

RanGDP comprises six stranded beta-sheets surrounded by six helices, where β_1, $\beta_{3\text{-}6}$ are parallel while β_2 is antiparallel. Every helix is a right-handed helical structure, and there are 13 loops that connect the mentioned secondary structural elements.

Like other small GTPases, the phosphate-binding loop (P-loop), together with a Mg^{2+} ion, plays a central role in stabilizing the bound nucleotide. In addition, the conserved structural elements switch I and switch II, both of which undergo major conformational changes in response to the GDP/GTP exchange (8). This conformational switching enables Ran to regulate the cargo loading/unloading of nuclear transport receptors (68).

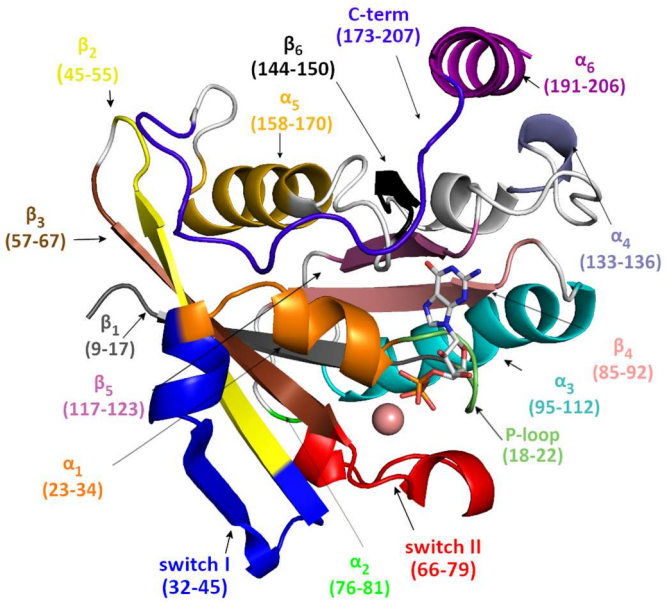

Figure 3. The secondary structure elements of Ran. *The GDP is shown as CPK, Mg^{2+} as vdW.* (69)

Switch I contains residues 32-45. In the GDP-bound (inactive) state, this region is an α-helix and a β-sheet structural element, whereas in the active GTP-bound form, it becomes less ordered, consisting of an α-helical segment followed by a flexible loop (Figure 4). The switch II region, spanning residues 66-79, adopts a loop followed by an α-helix in both nucleotide states. The P-loop corresponds to residues 18-23.

The structure of Ran consists of a G-domain (GTP binding domain) characteristic of small GTPases; however, in contrast to other GTPases, its C-terminal segment contains a distinct C-terminal helix. In the GDP-bound state, the C-terminus is associated with the G-domain (70, 71), while it is detached from it in the GTP-bound state (Figure 4). Notably, the full-length structure of RanGTP in the absence of binding partners has not been determined experimentally, as it has only been crystallized in macromolecular complexes (72-74). This region sequentially overlaps with the HVR of other members of the Ras superfamily. However, unlike those cases, where the HVR enables membrane association, in Ran it acts as a third switch (73, 75), by being attached or detached to the G-domain depending on the bound nucleotide.

In the crystal structures of RanGTP analogues in complex with RanBPs, the C-terminal region of Ran is resolved, embracing the RanBP (54, 76, 77). In macromolecular

complexes lacking RanBP, only the structure of the G-domain of RanGTP is determined, indicating a flexible C-terminus (78-81).

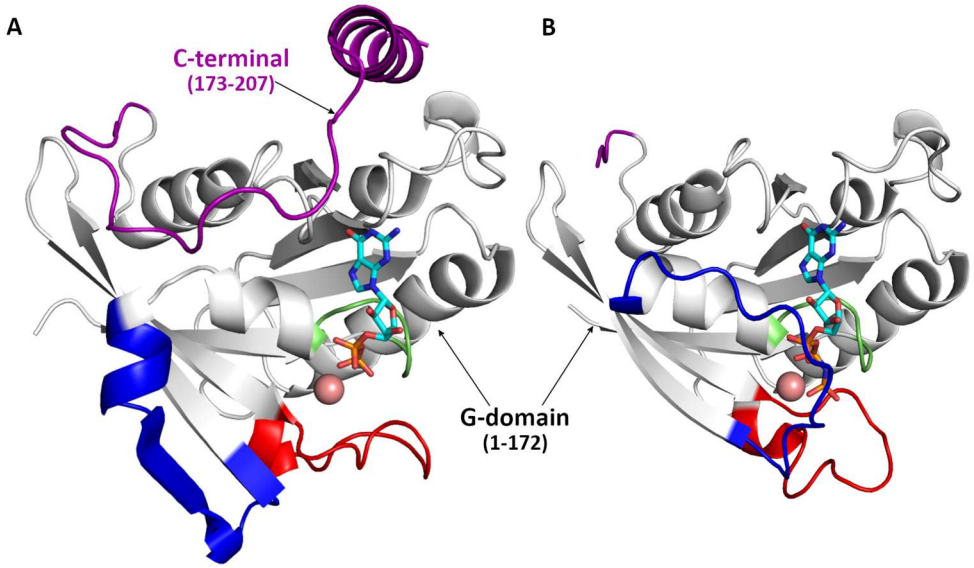

Figure 4. Representative crystal structures. *The crystal structure of RanGDP (A), and RanGTP (B). Different structural elements are color-coded: P-loop (lime), switch1 (blue), switch2 (red), C-terminal (purple), the GDP/GTP is denoted by CPK, Mg2+ by pink vdW. In GTP-bound conformation, the end of the C-terminal region is missing. (69)*

1.2. Simulation background

1.2.1. Molecular dynamics simulation method

Molecular dynamics (MD) simulation (82, 83) is one of the most widely employed computational approaches for studying macromolecules such as proteins and nucleic acids (84). It is used to examine the dynamics, thermodynamics, and conformational changes of macromolecules (85, 86). With modern computational power, MD can model these systems in conditions similar to their natural environment, typically in water (87-89). This, in turn, enables us to investigate numerous complex dynamical processes, such as the inner movements of proteins and DNA, conformational changes, enzyme reactions, and protein folding (90).

The principle of MD simulation

Consider an arbitrary system of N atoms under the Born-Oppenheimer approximation. The much smaller mass of electrons relative to nuclei leads to their rapid dynamical response. As a result, solving the electronic Schrödinger equation yields a

potential energy function, $U(\boldsymbol{r}_\mathrm{i})$, where $\boldsymbol{r}_\mathrm{i}$(with $i = 1, \ldots, N$) denotes the positions of the nuclei. The nuclear Schrödinger equation is then solved on this potential energy surface.

In molecular dynamics (MD) simulations (91), the following simplifications are introduced:

- Instead of solving the full electronic Schrödinger equation at each step, the potential energy function $U(\boldsymbol{r}_\mathrm{i})$ is replaced by an empirical energy function, known as a force field.
- Owing to their relatively large mass, atomic nuclei exhibit dynamics that are well described by classical mechanics, with their trajectories obeying Newtonian equations of motion:

$$m_\mathrm{i} \frac{\mathrm{d}^2 \boldsymbol{r}_\mathrm{i}(t)}{\mathrm{d}t^2} = \boldsymbol{F}_\mathrm{i} = -\nabla_{\boldsymbol{r}_\mathrm{i}} U \tag{1}$$

Force-field description

During a simulation, 3N coupled second-order ordinary differential equations must be integrated over time to obtain the trajectories of all atoms, thereby describing how their positions evolve. In classical MD simulations, the term force field (FF) refers to a set of mathematical functions and associated parameters that define the interactions between different types of atoms in various chemical environments (84). The total potential energy of the system is expressed as the sum of bonded and non-bonded interactions:

$$E_\mathrm{total} = E_\mathrm{bonded} + E_\mathrm{nonbonded} \tag{2}$$

when this equation is expanded, each term describes an atomic interaction:

$$E(r)_\mathrm{total} = \sum_{bonds} \frac{k_r}{2}(r - r_0)^2 + \sum_{angles} \frac{k_\theta}{2}(\theta - \theta_0)^2 + \sum_{tors.} \frac{k_\phi^{(n)}}{2}[1 + \cos(n\phi - \delta)] + \sum_{vdW} \left[\left(\frac{A_\mathrm{ij}}{r_\mathrm{ij}}\right)^{12} - \left(\frac{B_\mathrm{ij}}{r_\mathrm{ij}}\right)^{6}\right] + \sum_{electr.} \left(\frac{q_\mathrm{i} q_\mathrm{j}}{4\pi\varepsilon r_\mathrm{ij}}\right) \tag{3}$$

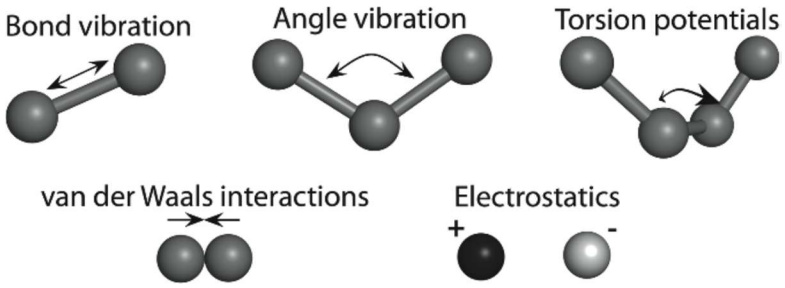

***Figure 5**. **Examples of interaction functions in modern force fields**. Bonded interactions include covalent bond-stretching, angle-bending, torsion rotation around bonds, and out-of-plane or "improper" torsions (not shown). Nonbonded interactions are based on neighbor lists and consist of Lennard-Jones attraction and repulsion as well as Coulomb electrostatics. The figure has been published by Kukol.* (92)

The first three terms represent the bonded interactions, whereas the last two terms correspond to the non-bonded interactions. The first term describes the bond-stretching energy between covalently bonded atoms, where k_r is the force constant for a bond of length r, and r_0 is the equilibrium bond length.

The second term accounts for bond-angle deformation, with k_θ denoting the angular force constant. Here, θ represents the angle between two covalent bonds, and θ_0 is the equilibrium angle.

The third term represents the energy associated with dihedral (torsional) angles, which captures the rotational barriers around covalent bonds. The periodicity of the potential is described by the cosine function, and δ is the phase angle. Although each torsional contribution is relatively small, the dihedral angles of the protein backbone (for example, around the Cα-N bond axis) are crucial for major conformational changes, as they determine the stable conformational states that give rise to functional loop rearrangements.

The fourth and fifth terms describe non-bonded interactions. These interactions are typically evaluated using a cutoff distance, beyond which their contributions are neglected. It is common practice to employ a shifted potential or a switching function to smoothly reduce the interaction energy to zero at the cutoff distance.

The fourth term models van der Waals interactions, typically using the Lennard-Jones potential. Here, A and B are atom-type-specific constants, and r_{ij} is the distance between atoms i and j.

The fifth term, $\frac{q_i q_j}{4\pi\varepsilon r_{ij}}$, describes the Coulombic (electrostatic) interactions between charged or polar atoms, where q_i and q_j are the atomic partial charges, r_{ij} is the distance between them, and ε is the permittivity.

The parameters of the force field —such as the spring constants k and equilibrium bond lengths r_0—are derived from ab initio quantum-mechanical calculations and experimental data, including X-ray crystallography and infrared spectroscopy.

Solving the equations of motion with integration algorithms

To calculate the trajectory, the function of the force-field potential is substituted into the right side of Newton's equation of motion:

$$m_{\mathrm{i}} \frac{\mathrm{d}^2 \boldsymbol{r}_{\mathrm{i}}(t)}{\mathrm{d}t^2} = -\frac{\partial E_{\mathrm{total}}}{\partial \boldsymbol{r}_{\mathrm{i}}} \tag{4}$$

To solve this, the *finite differential method* is used. The integration process is divided into infinitesimal small, equally sized time intervals δt, referred to as the time step. It is assumed that the force acting on each atom remains constant within each δt. The time step is chosen by the user but is ultimately constrained by the system being modeled. If it is too large, significant energy fluctuations may occur, causing instability. If it is too small, the computational cost becomes impractical. For flexible molecules such as proteins, the optimal time step is typically 1-2 fs, approximately one-tenth of the period of the highest-frequency motion in the system, namely the C-H bond vibration.

To calculate the dynamical behavior at each time step, second-order integration algorithms such as the Verlet (93), Velocity Verlet (94), and Leapfrog (95) methods are commonly employed in MD simulations. The Verlet algorithm uses the Taylor series expansion of the position vector **r**(t):

$$\boldsymbol{r}_{\mathbf{i}}(t+\delta t) = \boldsymbol{r}_{\mathbf{i}}(t) + \left(\frac{\partial \boldsymbol{r}_{\mathrm{i}}}{\partial t}\right)\delta t + \left(\frac{\partial^2 \boldsymbol{r}_{\mathbf{i}}}{\partial t^2}\right)\frac{\partial t^2}{2!} + \left(\frac{\partial^3 \boldsymbol{r}_{\mathrm{i}}}{\partial t^3}\right)\frac{\partial t^3}{3!} + \mathcal{O}(\boldsymbol{r}^4) \tag{5}$$

$$\boldsymbol{r}_{\mathbf{i}}(t-\delta t) = \boldsymbol{r}_{\mathbf{i}}(t) - \left(\frac{\partial \boldsymbol{r}_{\mathbf{i}}}{\partial t}\right)\delta t + \left(\frac{\partial^2 \boldsymbol{r}_{\mathbf{i}}}{\partial t^2}\right)\frac{\partial t^2}{2!} - \left(\frac{\partial^3 \boldsymbol{r}_{\mathbf{i}}}{\partial t^3}\right)\frac{\partial t^3}{3!} + \mathcal{O}(\boldsymbol{r}^4) \tag{6}$$

where

The sum of these equations, truncated at the third-order terms, gives the Verlet equation for the updated position vector:

$$\boldsymbol{r}_{\mathrm{i}}(t+\delta t) = 2\boldsymbol{r}_{\mathrm{i}}(t) - \boldsymbol{r}_{\mathrm{i}}(t-\delta t) + \left(\frac{\partial^2 \boldsymbol{r}_{\mathrm{i}}}{\partial t^2}\right)\partial t^2 = 2\boldsymbol{r}_{\mathrm{i}}(t) - \boldsymbol{r}_{\mathrm{i}}(t-\delta t) - \frac{\partial t^2}{m_{\mathrm{i}}}\frac{\partial E_{\mathrm{total}}}{\partial \boldsymbol{r}_{\mathrm{i}}} \quad (7)$$

The velocity formula can be similarly determined:

$$\boldsymbol{v}_{\mathbf{i}}(t) = \frac{\boldsymbol{r}_{\mathbf{i}}(t+\delta t) - \boldsymbol{r}_{\mathbf{i}}(t-\delta t)}{2\delta t} = \frac{\boldsymbol{r}_{\mathbf{i}}(t) - \boldsymbol{r}_{\mathbf{i}}(t-\delta t)}{\delta t} - \frac{\partial \mathrm{t}}{2m_{\mathrm{i}}}\frac{\partial E_{\mathrm{total}}}{\partial \boldsymbol{r}_{\mathrm{i}}} \quad (8)$$

The temperature can be obtained by:

$$T(t) = \frac{1}{(3N-n)k_B}\sum_{i=1}^{N} m_{\mathrm{i}} v_{\mathrm{i}}^2(t) \quad (9)$$

1.2.2. Molecular Dynamics with Excited Normal Modes

Due to the large number of degrees of freedom, proteins can adopt a vast array of conformations, resulting in a highly complex potential energy landscape. Considering the enormous ensemble of conformations in dynamic equilibrium in solution, a detailed investigation of protein dynamics is computationally expensive. Consequently, numerous methods have been developed to improve the conformational sampling of biomolecules.

MDeNM (Molecular Dynamics with excited Normal Modes) (96) is an enhanced MD simulation technique that provides the advantage of accelerating conformational transitions without altering the potential energy surface in a way that would artificially displace the system from one energy minimum to another, unlike some other accelerated methods. Instead, MDeNM injects energy along predefined directions, promoting transitions over energy barriers while preserving the underlying energy landscape.

The working principle of MDeNM is as follows (Figure 6.): a classical MD simulation is performed on the system, and the normal modes (NMs) of the energy-minimized structure are calculated. This involves diagonalization of the full mass-weighted molecular Hessian matrix, which can be carried out using various methods depending on the simulated system (97, 98). A random linear combination of biologically relevant low-frequency modes ($\boldsymbol{q_i}$) - specifically those whose directions overlap with the conformational changes of interest - is then generated ($\boldsymbol{Q} = \sum_{i=1}^{n} \alpha_i \boldsymbol{q}_i$ where α_i are uniformly distributed coefficients). These modes, corresponding to the lowest

eigenvalues of the Hessian matrix, represent large-amplitude, global motions that are most likely to contribute to the biological phenomenon under investigation (99, 100). The resulting vector defines the direction of excitation, which differs for each replica. To ensure adequate sampling of the conformational space, the number of replicas is increased with the dimensionality of the NM space. Additional velocities are then applied along the corresponding vectors to introduce kinetic energy into the system. The excitation direction determines the excitation factor, which is set based on a user-defined excitation temperature; the optimal value depends on the system and the amplitude of the motion of interest and is typically determined empirically, with values generally in the 10–50 K range. Finally, the Cartesian atomic velocities corresponding to the NM space are added to those obtained at the last step of the previous simulation. A short classical MD run is subsequently performed to dissipate the injected energy and restore equilibrium. This procedure constitutes one replica and can be repeated iteratively, allowing the system to explore conformational wells that are rarely sampled in conventional MD due to timescale limitations.

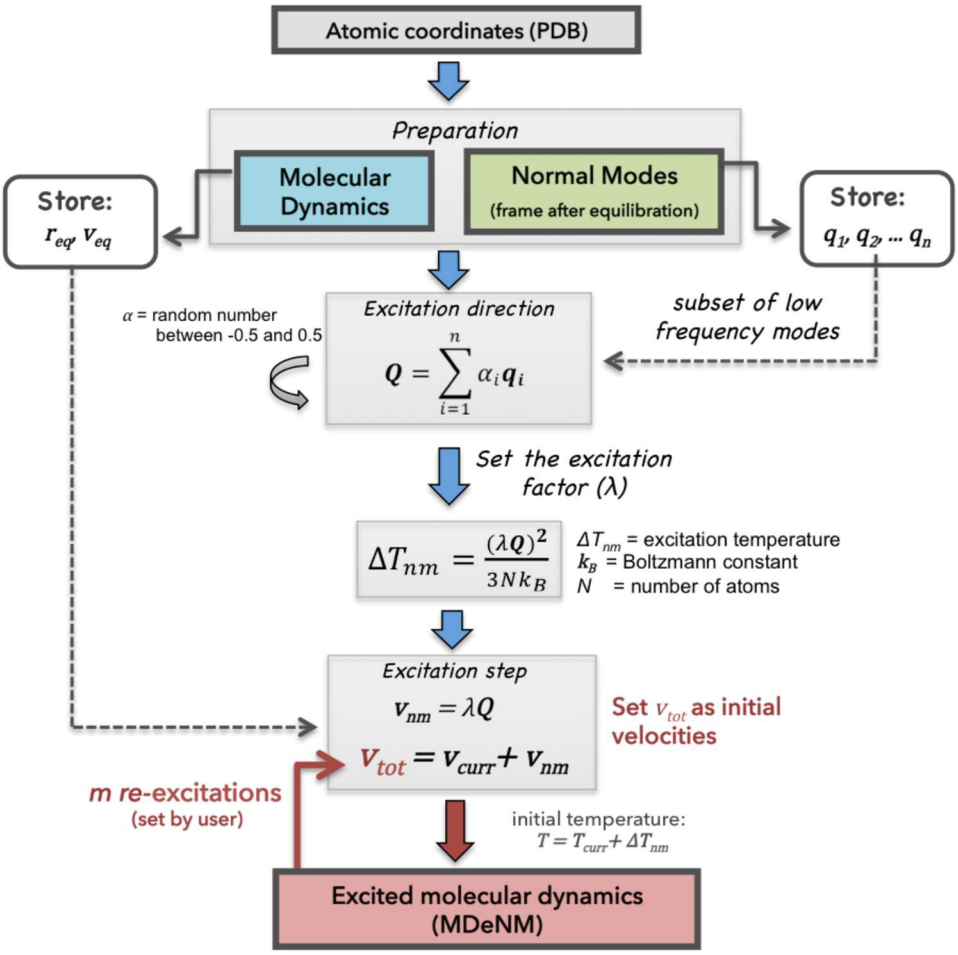

Figure 6. Flowchart of the MDeNM procedure*. After the preparation step, a random linear combination of NM vectors is used to generate the vector* ***Q****. An excitation factor (λ), based on the user-defined* ΔT_{nm}*, is calculated, and the corresponding velocity along* ***Q*** *is added to the current velocities (*v_{curr}*). The system subsequently undergoes an excited dynamics simulation (MDeNM). Initial velocities and coordinates are taken from equilibration MD, while re-excitations use the final state of the preceding MDeNM run. The figure has been published by Costa et al.* (96)

MDeNM allows efficient exploration of the dynamic equilibrium of macromolecules without introducing bias in the potential energy terms. By periodically applying additional energy along selected low-frequency normal modes (or linear combinations thereof), the method promotes motion along directions that facilitate large-scale conformational changes, such as domain allosteric transitions.

However, certain limitations must be taken into account. Excessive kinetic energy input can lead to structural distortions or neglect the effects of the environment on conformational transitions. Additionally, because MDeNM explores directions defined by combinations of normal modes, structural and environmental contributions to the directionality of motion may be underestimated or overlooked.

Adaptive Molecular Dynamics with Normal Mode Excitation

An alternative approach involves modifying and adapting the directions of NM vectors during displacements to reduce tensions arising from internal anharmonicities and environmental effects, thereby allowing larger conformational changes to occur with minimal stress. This approach, referred to as adaptive collective motions, has been implemented within the framework of the MDeNM method, in which a linear combination of initial modes calculated in vacuum is used to propagate movements over larger distances in a complete system, including the full environment (e.g., water, membrane) (101). Small adaptive modifications in the directions of collective movements enable a more extensive exploration of the conformational space, leading to structural changes that would not be achievable if only the original NM vectors were employed. Directional adjustments primarily occur when low- and medium-frequency motions are intrinsically activated during the trajectories.

To maintain the system in a continuously excited state, the kinetic energy along the excitation vector is periodically evaluated and adjusted as needed. Because the added energy dissipates rapidly, the velocity along the excited direction is rescaled at the end of each excitation to maintain a constant energy level:

$$\boldsymbol{v}_{\mathrm{p}} = \frac{(\boldsymbol{v}_{\mathrm{curr}} \cdot \boldsymbol{Q})}{|\boldsymbol{Q}|^2} \cdot \boldsymbol{Q},\ \boldsymbol{E}_{\mathrm{k}} = \frac{1}{2}\left(\bar{\bar{\boldsymbol{M}}}^{\frac{1}{2}}\boldsymbol{v}_{\mathrm{p}}\right)^2, \boldsymbol{v}_{\mathrm{new}} = \boldsymbol{v}_{\mathrm{curr}} + \left(\boldsymbol{v}_{\mathbf{exec}} - \boldsymbol{v}_{\mathbf{p}}\right) \qquad (10)$$

where $\boldsymbol{v}_{\mathrm{curr}}$ is the current velocity vector, $|\boldsymbol{Q}|^2$ is the norm vector of $\boldsymbol{Q}$ and $\bar{\bar{\boldsymbol{M}}}$ is the mass matrix. $\boldsymbol{v}_{\mathbf{exec}}$ is constant excitation energy input which is defined by the user. The above equation obtains the new excitation velocities to inject.

Because $\mathbf{Q}_n$ is based on the initial structure, its direction becomes less representative after successive excitations due to anharmonic effects. To prevent structural distortions, excitation directions are updated based on the trajectory evolution. The mass-weighted difference vector is:

$$\mathbf{d}_{\mathrm{n}} = \mathbf{M}^{\frac{1}{2}}\langle\mathbf{r}\rangle - \mathbf{r}^0, \cos(\alpha) = \frac{\mathbf{d}_{\mathrm{n}}}{|\,\mathbf{d}_{\mathrm{n}}\,|} \cdot \mathbf{Q}_{\mathrm{n}} \qquad (11)$$

The excitation vector is updated when the displacement along $\mathbf{Q}_n$ exceeds a threshold ℓ and $\cos\alpha \leq 0.5$. Otherwise, the previous vector is retained. Formally:

$$\mathbf{Q}_{n+1} = \begin{cases} \mathbf{d}_n, \text{ if } \alpha_n \leq 60^\circ \\ \mathbf{Q}_n, \text{ if } \alpha_n > 60^\circ \end{cases} \quad (12)$$

Updates are applied only when both the displacement and directional change are sufficiently large to exceed normal fluctuations, ensuring simulation accuracy. Figure 7 illustrates the excitation vector correction along MDeNM simulations.

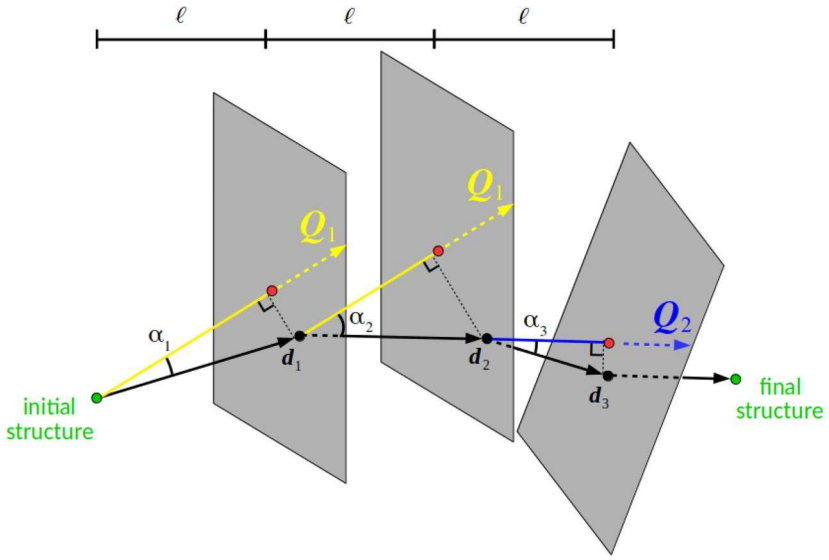

Figure 7. Adaptive correction of excitation vector during MDeNM simulations. *The vectors* $\boldsymbol{Q_1}$ *and* $\boldsymbol{Q_2}$ *are excitation directions, while* $\boldsymbol{d_{1\text{-}3}}$ *are the corresponding displacement vectors. When a set MRMS threshold (ℓ) is reached, the program checks whether to update the direction. If cos* $\alpha_n \leq 0.5$ *(i.e., deviation > 60°), the excitation direction is changed; otherwise, it stays the same. Here, cos* $\alpha_1 \geq 0.5$ *keeps* $\boldsymbol{Q_1}$ *unchanged, but cos* $\alpha_2 < 0.5$ *updates the direction to* $\boldsymbol{Q_2} = \boldsymbol{d_2}$*, allowing exploration of new motion directions influenced by the medium. The figure has been published by Resende-Lara et al.* (101)

The aMDeNM workflow is summarized in Figure 8. The preparation step involves a short MD simulation and calculation of the normal modes of the minimized structure, yielding the initial positions ($\mathbf{r}_{eq}$), velocities ($\mathbf{v}_{eq}$), and directions for excitation ($\mathbf{q}_{1\ldots n}$). The excitation vector $\mathbf{Q}$ is then generated as a random linear combination of these modes. In a multi-replica setup, each replica has a distinct $\mathbf{Q}$ vector, which is filtered using root-mean square distance (RMSD) to retain only sufficiently distinct vectors. Each retained vector is scaled by a user-defined factor λ to set the excitation energy ΔE, producing excitation velocities $\mathbf{v}_{ex}$ that are added to $\mathbf{v}_{eq}$. During the simulation, the energy along $\mathbf{Q}$ is periodically evaluated and rescaled if needed, and the real displacement direction is compared with the theoretical vector. If a deviation greater than 60° is detected, the excitation vector is updated accordingly.

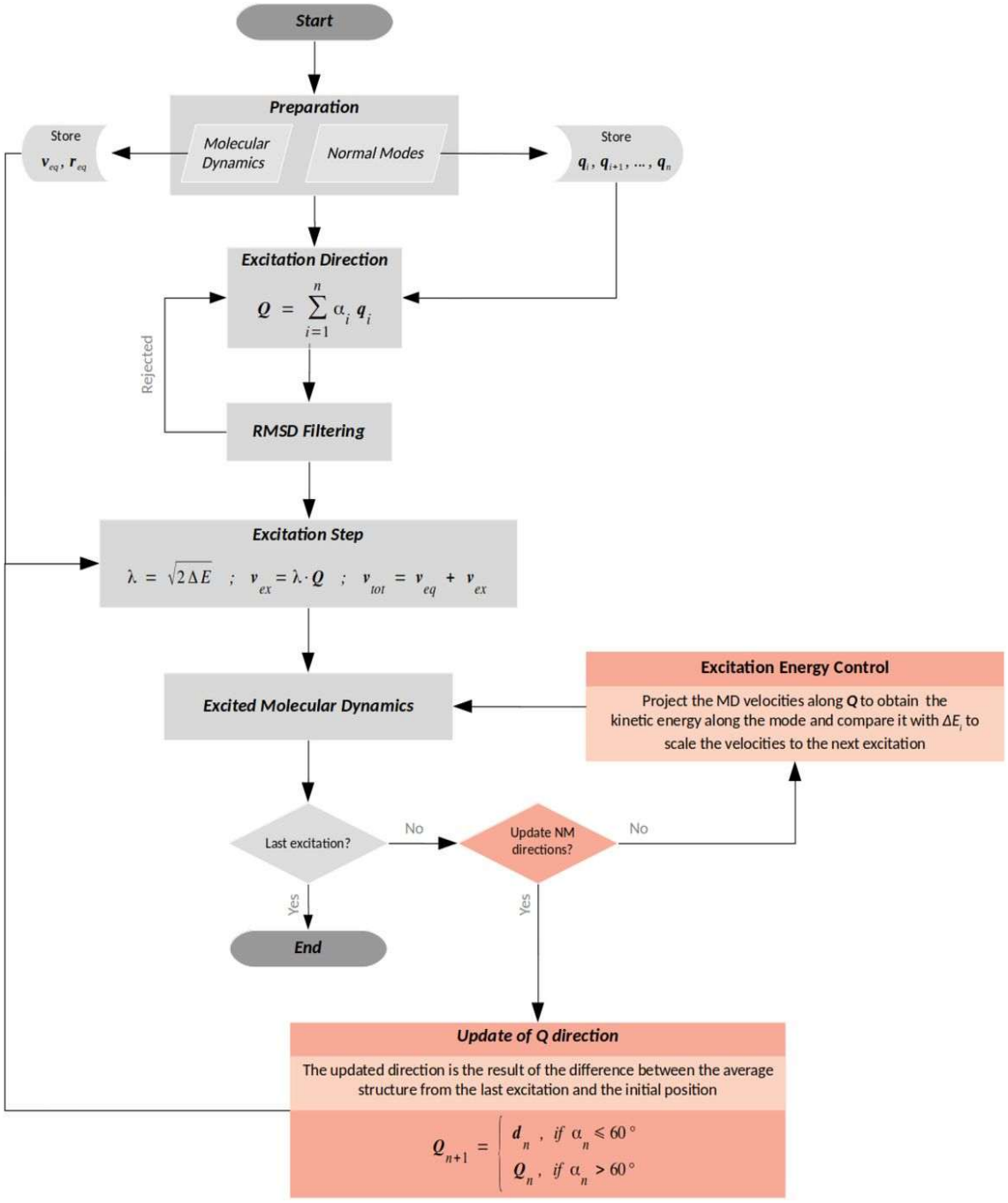

Figure 8. aMDeNM flowchart with the new implementations. *Schematic overview of the excitation protocol, in which normal-mode analysis generates excitation vectors that are filtered, energy-scaled, and added to the equilibrated velocities before simulation, with periodic rescaling and direction updates during the run. The figure has been published by Resende-Lara et al.* (101)

2. OBJECTIVES

The overarching objective of this research is to elucidate the molecular mechanisms underlying the nucleotide specificity and binding in the human small GTPase Ran.

Objective 1: Exploration of Structural Dynamics of RanGDP and RanGTP

We aim to characterize and compare the structural and dynamic properties of Ran in its GDP- and GTP-bound states, with particular emphasis on conformational flexibility, nucleotide-dependent behavior, and determinants of nucleotide specificity, using MD and aMDeNM simulations.

Objective 2: Impact of C-terminal movement of RanGTP on ligand binding

We aim to investigate the functional implications of the highly flexible and frequently unresolved C-terminal region of RanGTP, and to determine how its conformational mobility influences ligand recognition and binding.

Objective 3: Investigation of switch I opening of RanGTP

We aim to define and characterize the molecular mechanism underlying switch I opening in RanGTP by reproducing the observed conformational transition in simulations and identifying the key interactions and perturbations that trigger this process.

3. METHODS

3.1. Structure preparation

The starting structure of RanGDP was obtained from the Protein Data Bank (102) (PDB ID: 5CIQ) (103), based on the human crystal structure. For human RanGTP, the crystal structure with PDB ID 5CLL (103) was used. Since this RanGTP structure is incomplete in the C-terminal region, the missing segment (residues 185-207) was modeled using coordinates from PDB ID 5CLQ. This structure was not chosen as the primary model due to the Y39A mutation, but it provided a suitable template for completing the missing C-terminal segment by aligning residues 176-184. The 5CLL structure was chosen for modeling the G-domain since it contains GDP–BeF, a transition-state analogue, whereas 5CLQ represents a non-hydrolysable GTP-bound form.

Although the last six residues of RanGDP (residues 210-216, sequence DEDDDL), known as the "acidic tail," are theoretically involved in interactions with the basic patch of the G-domain (residues 139-142), they were not resolved in the crystal structure, likely due to their high flexibility. To avoid introducing structural bias, this tail was not modeled in either RanGDP or RanGTP structures. Additionally, the GDP-BeF analogue present in the original structure was modified to GTP.

The protonation states of the proteins were determined using PROPKA (104) at pH 7.0. All residues exhibited standard pK values. Histidine residues in both structures were singly protonated at either the δ- or the ε-nitrogen, with assignments made based on their local structural environments.

All starting structures were solvated using the CHARMM-GUI (105-108) web tool. For the RanGDP system, a cubic simulation box containing TIP3P water molecules was constructed with dimensions of 78 × 78 × 78 Å, ensuring a minimum distance of 14 Å between the protein surface and the box boundaries to avoid self-interactions across periodic boundaries. A similar cubic box was generated for the RanGTP system; however, due to the anticipated significant conformational change associated with the C-terminal helix, the box dimensions were increased to 128 × 128 × 128 Å, providing at least 39 Å of solvent padding. In both systems, the NaCl concentration was set to 0.15 mol/L.

For energy calculations, the dielectric constant was set to 1. Electrostatic interactions were computed using the Particle Mesh Ewald (PME) method (109), with a grid spacing of 1 Å or less, resulting in an order of magnitude of 6. The real-space component of the electrostatics was truncated at a cutoff distance of 12.0 Å, and the width of the Gaussian charge distribution was set to 0.34 $Å^{-1}$. Van der Waals (vdW) interactions were smoothly truncated using a switching function that operated between 10.0 and 12.0 Å, reducing the vdW forces to zero at the cutoff distance.

Each solvated system was subjected to a multi-stage energy minimization protocol. Initially, harmonic restraints were applied to the Cartesian coordinates of all heavy atoms, with a gradually decreasing force constant. Minimization began with steepest descent (110) for 1,500 steps, during which the restraint force constant was reduced in three stages: 10, 1, and 0.1 kcal/mol/$Å^2$, each over 500 steps. This was followed by 200 steps of conjugate gradient minimization with a force constant of 0.1 kcal/mol/$Å^2$. Finally, an unrestrained minimization was performed in three stages: 100 steps of steepest descent, 200 steps of conjugate gradient, and 1,000 steps using the adopted basis Newton-Raphson (ABNR) method (111). Minimization was executed using the CHARMM (105, 112) software with the CHARMM C36m force field (113, 114).

To reproduce the opening behavior of RanGTP, as further described in the Results section, potential driving structural features were identified, and a series of modified or alternative structures were simulated to investigate the underlying mechanism. An overview of the performed simulations is provided in Table 1. and the structures used for this purpose are shown in Figure 9.

3.1.1. Reproduction of switch I opening

To reproduce the opening of switch I observed in our initial simulations, we employed two separate approaches.

First, we selected the structure from 103 ns into the simulation—a few ns preceding the switch I opening event (Figure 9A)—and initiated seven parallel simulations from this snapshot, each with different initial velocity distributions.

Second, after identifying interactions that affect the stabilization of switch I, harmonic distance constraint was applied between the atoms of the interacting amino acids (Lys152:NZ-Glu186:OE2), gradually bringing them to a distance of 3.4 Å,

matching the interaction observed in the RanGDP crystal structure (PDB: 5CIQ; Figure 9B).

3.1.2. Magnesium ion coordination structure

To investigate the effect of Mg^{2+} coordination on the opening of switch I, we used the 5CLL crystal structure of RanGTP, supplemented with the conformation of the C-terminus from the initial simulation at 20 ns (Figure 9C). This choice ensured that Mg^{2+} coordination remained as defined by the crystallographic structure. This combined structure was solvated using CHARMM-GUI within a rectangular water box with dimensions of 85 × 85 × 85 Å, extending 14 Å beyond the molecular surface in all directions, with 0.15 mol/L NaCl concentration. Due to the artifact observed with the previously used energy minimization protocol (see Results), a revised protocol was employed in which harmonic restraints were applied to all heavy atoms. Throughout 10,000 minimization steps, the Cartesian coordinates of these atoms were constrained with force constants of 1.0 kcal/mol/Å² for backbone atoms and 0.5 kcal/mol/Å² for side chains.

Following minimization, a 20 ns molecular dynamics simulation was conducted, during which a harmonic distance restraint was applied between the NZ atom of Lys152 and the OE2 atom of Glu186. The equilibrium distance of this restraint was gradually decreased to 3.4 Å, mimicking the proximity observed in the RanGDP structure, with a force constant of 20 kcal/mol/Å².

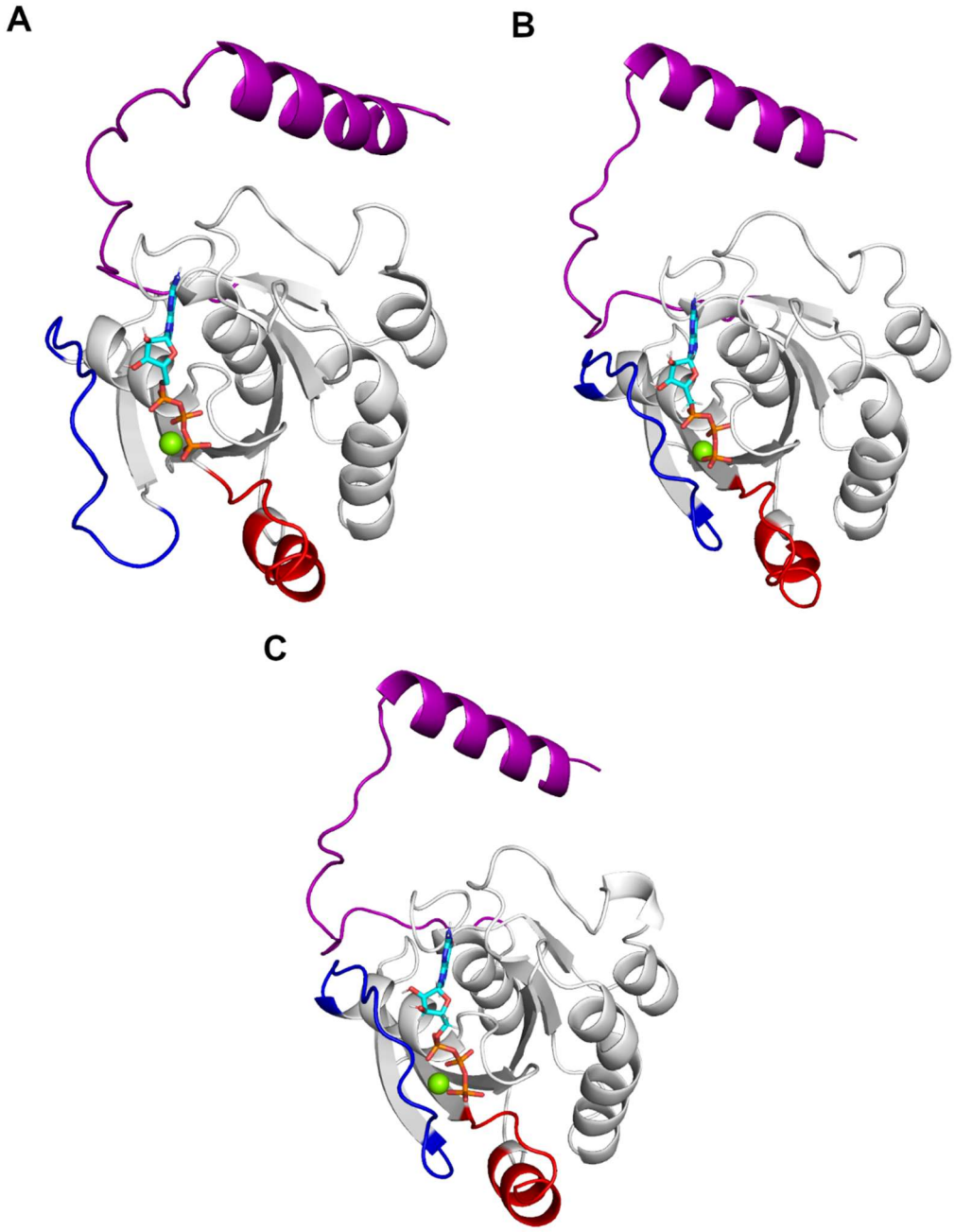

Figure 9. Starting structures of MD simulations. *The structure of RanGTP at the end of the 103rd ns of md1 simulation used as a starting structure of the md' simulations (**A**); the structure of RanGTP at the end of the 20th ns of md1 simulation used as a starting structure of the md_constr152 simulations (**B**); the crystal (5CLL) structure of RanGTP, completed with the conformation of the C-terminus of the md1 20th ns simulation (**C**). switch I is colored blue, switch II red, the C-terminus purple, GTP is represented by sticks, and the Mg^{2+} by a sphere. (115)*

3.2. MD and MDeNM simulations

3.2.1. MD

The energy-minimized structures were first equilibrated by a 200 ps NVE simulation at 300 K, followed by a 5 ns NPT equilibration at 1 atm. Langevin dynamics was employed with a damping coefficient of 1 ps^{-1}, a piston oscillation period of 50 fs, and a piston decay time of 25 fs. An integration time step of 2 fs was used throughout the simulation. Prior to the NVE equilibration step, random velocities were assigned to atoms according to the Maxwell-Boltzmann distribution at 300 K.

As shown in Table 1., in the first set of simulations, 200 ns production runs were carried out starting from the equilibrated structures of RanGDP and RanGTP, with frames saved every 20 ps. The parameters for the production runs were identical to those used during the 5 ns NPT equilibration. After observing the switch I opening behavior, these simulations were extended to 1 μs.

A second set of 1 μs simulations was initiated from the structures shown in Figure 9A (five parallel simulations, labeled *md'*) and Figure 9B (three parallel simulations, labeled *md_constr152_*).

Lastly, based on the structure in Figure 9C, five parallel 1 μs MD simulations were performed using an upper wall restraint between the amino group of Lys152 and the OE1/OE2 atoms of Glu186. This restraint applied a force constant of 20 kcal/mol/$Å^2$ for distances exceeding 4 Å. Following these runs, an additional restraint was introduced on the final structures: a distance constraint between the OG2 atom of Thr42 and the Mg^{2+} ion, increasing their separation up to 10 Å, thereby excluding Thr42 from the Mg^{2+} coordination sphere. From these modified structures, a final set of five 1 μs unrestrained simulations was performed.

3.2.2. aMDeNM

In the first set of simulations, aMDeNM simulations were performed to efficiently explore the conformational space of the C-terminus. The normal modes required for these simulations were computed in vacuum using the final structures obtained from the 5 ns equilibration runs of both GDP- and GTP-bound forms.

Prior to normal mode analysis, energy minimization was carried out using the steepest descent algorithm, with harmonic positional restraints gradually reduced in four steps: 10, 1, 0.1, and 0 kcal/mol/Å², each applied for 1,000 steps. This was followed by 50,000 steps of minimization using the adopted basis Newton-Raphson method. Normal mode calculations were then performed using the VIBRAN module of CHARMM (116).

For the closed RanGDP structures, no low-frequency normal modes were identified that would facilitate opening of the C-terminus; therefore, aMDeNM simulations could not be applied in this case. In contrast, for the RanGTP structure, four low-frequency normal modes were selected based on their root-mean-square fluctuation (RMSF) contributions. The final structure from the 5 ns equilibration was used as the starting point for the aMDeNM simulations.

To generate excitation directions, randomized linear combinations of the four selected modes were created. To ensure the diverse sampling of conformational space, new excitation directions were only accepted if the root-mean-square deviation (RMSD) between structures displaced by 1 Å along the new mode combination and any previously accepted mode combination was greater than 1.15 Å. This filtering resulted in 183 unique excitation directions, each used to initiate a separate aMDeNM replica simulation.

In each replica, the system was kinetically excited along the corresponding mode combination using successive short MD simulations of 0.2 ps, with a sustained energy input of 1.25 kcal/mol per excitation. Each excitation-relaxation cycle produced one conformation. With 200 excitation cycles per replica, a total of 36,600 structures were generated across all simulations.

System	Name	Type	Eq. bias	Prod. bias	Time
RanGDP	*md1-md3*	MD	∅	∅	(3 × 200 ns) 3 × 1 µs
RanGTP	*md1-md3*	MD	∅	∅	(3 × 200 ns) 3 × 1 µs
	md1'-md7'	MD	∅	∅	7 × 1 µs
	md_constr152_1 *- md_constr152_3*	MD	20 ns long, Lys152-Glu186	∅	3 × 1 µs
	md_mgoct_152_1- *md_mgoct_152_5*	MD	20 ns long, Lys152-Glu186	Upperwall Lys152-Glu186	5 × 1 µs
	md_152_mg42_1- *md_152_mg42_5*	MD	20 ns long, Thr42 - Mg^{2+}	∅	5 × 1 µs
	MDeNM	aMDeNM	∅	∅	183 × 0,2 ns

Table 1. Summary of simulations performed for Ran in GDP- and GTP-bound states. *Traditional MD simulations were run from multiple replicas, some systems with initial 200 ns segments followed by extended 1 µs production runs. Additional biased simulations targeted key interactions during equilibration, with either unbiased or restrained production phases and enhanced sampling using aMDeNM to explore collective motions.*

3.3. Quantitative analysis

Root Mean Square Fluctuation (RMSF)

Root Mean Square Fluctuation (RMSF) provides a quantitative measure of the average positional deviation of each atom from its mean position over the course of a molecular dynamics simulation. This metric is commonly used to distinguish between rigid and flexible regions within a protein structure, independent of the time ordering of frames. The RMSF for atom *i* is calculated using the following formula:

$$RMSF_{\mathrm{i}} = \sqrt{\sum_{t_j=1}^{T} \frac{\left(x_{\mathrm{i}}(t_{\mathrm{j}}) - \overline{x_{\mathrm{i}}}\right)^2}{T}} \quad (13)$$

Where:

- $x_{\mathrm{i}}(t_{\mathrm{j}})$ is the position of atom i at time point t_j,
- $\overline{x_{\mathrm{i}}}$ is the time-averaged position of atom i over the entire trajectory,
- T is the total number of frames in the trajectory.

To reduce noise and computational complexity, the analysis was restricted to the Cα atom of each amino acid residue, which provides a reliable representation of backbone fluctuations.

3.3.1. Interaction energy analysis

To assess the energetic contributions of inter-segment interactions within the protein, pairwise non-bonded interaction energies were calculated using the CHARMM program. This analysis focused on quantifying van der Waals and electrostatic interactions between residues located in different structural segments of the protein. Only residue pairs in close spatial proximity (within 12 Å) were considered, allowing for the identification of physically relevant contacts that are likely to contribute to structural integrity or dynamic transitions. For each selected residue pair, the non-bonded interaction energy was computed while excluding bonded and intra-residue terms.

All interaction energy calculations were performed using the CHARMM C36m force field, consistent with the parameters applied in the production molecular dynamics simulations.

3.3.2. Inter-residue distance calculations

To evaluate potential interactions between specific regions of the protein and a ligand or between different protein segments, minimum distances between selected atom groups were calculated using CHARMM. Typically, side chain heavy atoms of a residue or segment—excluding backbone atoms—were compared to relevant heavy atoms of the ligand or interacting segment. Distances below a threshold of 5,5 Å were considered indicative of direct interactions or contacts. These distance measurements were recorded

throughout the simulations to monitor the formation, persistence, or disruption of key interactions, thereby providing insight into conformational dynamics and functional mechanisms.

3.3.3. C-terminus visualization with coordinate transformation

To facilitate the analysis of protein segment dynamics, the structure was transformed such that its principal geometric axes were aligned with the coordinate axes: the principal axis of largest moment of inertia was aligned with the z-axis, and the second-largest with the x-axis. Prior to this transformation, the system was translated so that a selected reference atom—the Cα atom of a defined residue—was positioned at the origin (0, 0, 0). This ensured that the analysis was centered on a biologically relevant point.

Following alignment, the radius of gyration and mass-weighted center of mass of the defined protein segment were calculated for each frame of the simulation. These coordinates were recorded together with the frame identifier to track the segment's position and conformational changes relative to the transformed coordinate system throughout the trajectory.

4. RESULTS

4.1. Nucleotide-dependent functional dynamics of full-length Ran

4.1.1. Structural study

A series of MD and aMDeNM simulations were carried out to gain a deeper understanding of the structural dynamics of the two conformations of the small GTPase Ran. Our goal was to explore the effect of different ligand binding on the two forms and the C-terminal movement of RanGTP.

To examine the dynamic behavior of the previously identified structural elements, the RMSF values for the Cα atoms of both structures in all MD simulations are presented in Figure 10. As previously known from literature, during the MD simulation, the fluctuation of the C-terminus is increased in the GTP-bound form (Figure 10A). Unexpectedly, in contrast to the K-Ras protein (117), RanGTP shows a higher fluctuation of the switch I region compared to RanGDP. Similarly to the K-Ras structures, the GDP/GTP exchange rigidifies the switch II region.

Figure 10B compares the two simulation methods, MD and aMDeNM, through the fluctuation values of RanGTP. The graph shows that applying aMDeNM results in increased fluctuation of the C-terminus region compared to conventional MD simulation, implying that the C-terminus samples a more extensive conformational landscape with aMDeNM. As detailed in the Method section, given that no normal mode was found to open the C-terminus of the closed RanGDP structure, it was not possible to perform aMDeNM on the GDP-bound structure. This observation further suggests that RanGDP has a stable, relatively rigid conformation. Another notable difference between the MD and aMDeNM simulations of RanGTP is the absence of switch I fluctuations in the aMDeNM results. This may be attributed to the selection of the four normal modes used in the aMDeNM calculations, which were used primarily to emphasize motions of the C-terminus.

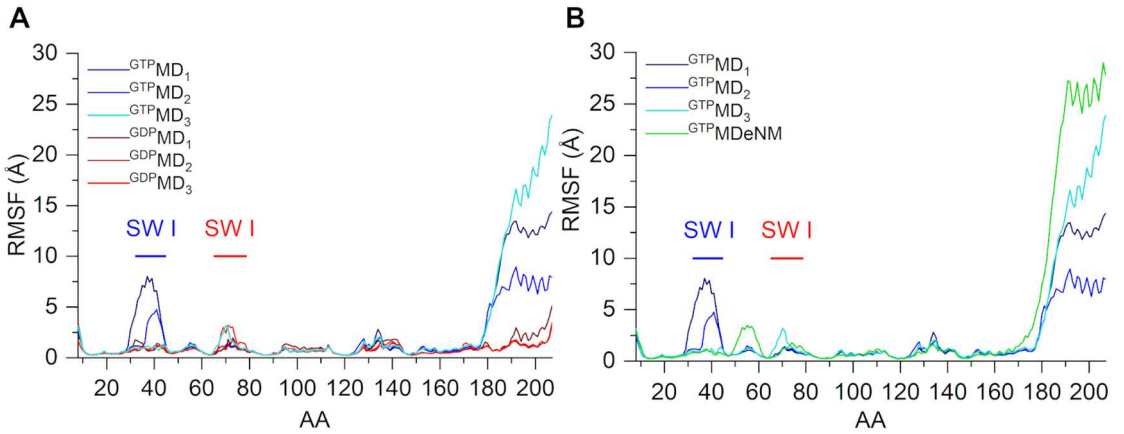

Figure 10. RMSF values during the simulations. *RMS fluctuation values of C_α atoms during MD of RanGDP (shades of red) and RanGTP (shades of blue) (**A**); and of RanGTP during MD (shades of blue) and MDeNM (green) simulation (**B**). (69)*

4.1.2. Mapping of the possible C-terminal conformations

To get a clearer visualization of the C-terminal movement relative to the G-domain, a coordinate transformation was applied throughout the trajectories, such that the position of the origin of the coordinate system was at the base of the C-terminal tail region (at residue 177). The Z-axis was aligned with the axis corresponding to the largest moment of inertia of the C-terminus. It was oriented away from the G-domain, with the x-y plane defined as perpendicular to it. The center of mass (COM) of the C-terminal α-helix was calculated within this coordinate system. The z-coordinate values reflect the displacement of the C-terminal tail along the Z-axis, with positive values indicating movement away from the G-domain and negative values indicating movement toward it. The x-y coordinates represent the lateral positioning of the C-terminus relative to the G-domain, indicating which side it occupies.

Figure 11B illustrates that the C-terminus of RanGDP remains confined to a stable position across all three MD simulations. The starting structure from Figure 11A is denoted by a pink mark in Figure 11B. The COM positions of the C-terminus from known experimental RanGDP structures are indicated by green markers (PDB IDs: 2MMC, 2N1B (118), 3CH5 (119), 3GJ0, 3GJ3 (120), 5CIQ, 5CIT (103)), highlighting the consistent and well-defined position of the C-terminal tail with respect to the G-domain in these structures.

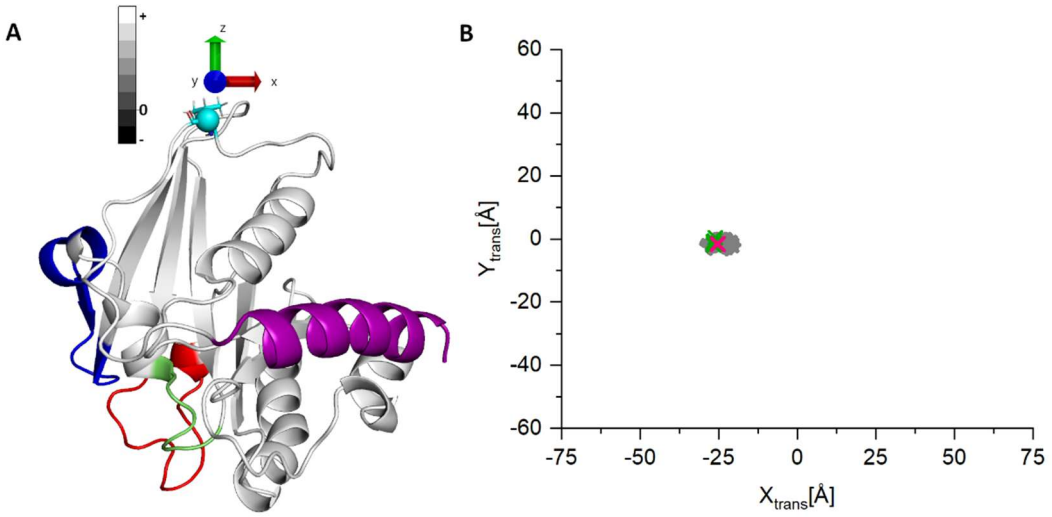

Figure 11. Two-dimensional representation of the center of mass of the C-terminal helix of RanGDP. *The starting structure for the MD simulations of RanGDP after the coordinate transformation. The origin of the coordinate system is defined at the base of the C-terminal tail (residue 177, shown as a cyan sphere); switch I, switch II, and the P-loop are colored blue, red, and green, respectively (**A**); the coordinates of the center of mass (COM) of the C-terminal helix on the x-y plane (**B**). The points are gray-scale-coded by their z-coordinate values. The pink mark denotes the starting structure; the green marks the coordinates of the other experimentally determined structures. (69)*

Figure 12 presents the positions of the C-terminus of RanGTP during the three MD simulations and the aMDeNM trajectories. As in previous figures, the starting structure is a pink mark (Figure 12A) and experimental RanGTP structures are indicated by green markers (PDB IDs: 1K5D, 1K5G (48), 1RRP (73), 4GPT (121), 4HAT, 4HB4 (53), 4WVF (122), 5DI9, 5DIF (123), 5UWI, 5UWP, 5UWT, 5UWU (124), 6LQ9 (125), 6X2M, 6X2O, 6X2R, 6X2S, 6X2U, 6X2W, 6X2X, 6X2Y (126), 6XJP, 6XJT, 6XJW (127)). In all three MD simulations (Figure 12B-D), the initially open C-terminal conformation explores either a relatively confined region of the conformational space (simulations 1 and 2; Figure 12B and C) or a broader range (simulation 3; Figure 12D) before ultimately adopting a more stabilized conformation by closing onto different regions of the G-domain surface.

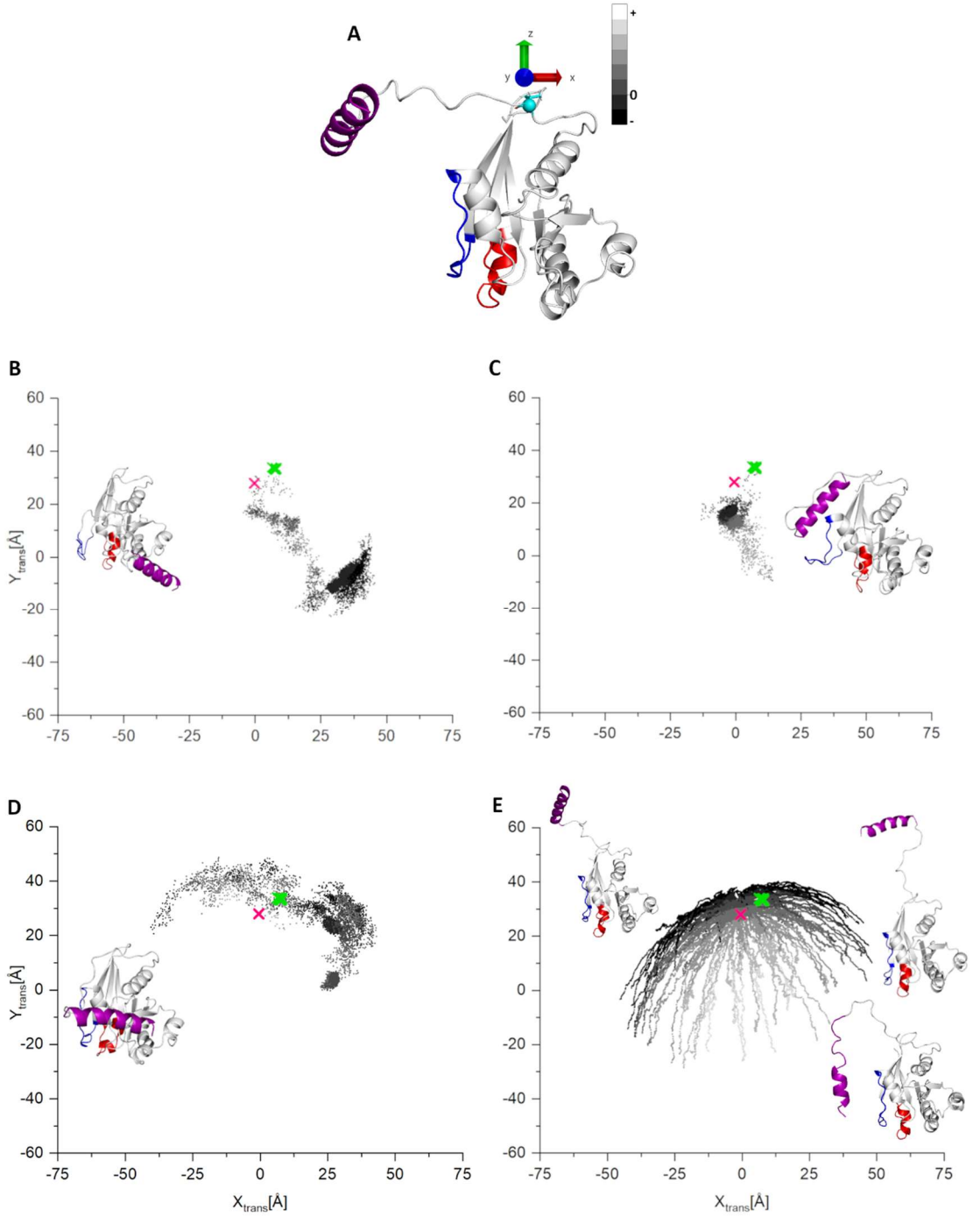

Figure 12. Two-dimensional representation of the COM of the C-terminal helix of RanGTP. *The starting structure for the simulations after the coordinate transformation is shown with the origin at residue 177 (cyan sphere); switch I and II are colored blue and red (**A**); The coordinates of the COM of the C-terminal helix on the x-y plane of the three parallel MD simulations (**B-D**); the result of the MDeNM simulation (**E**). The points are gray-scale-coded by their z-coordinate values. The pink mark denotes the starting structure; the green marks the coordinates of the other experimentally determined structures. In the inset, the final structures of the three MD simulations are represented. While for the MDeNM part (**E**), some representative structures are shown. (69)*

4.1.3. Key interactions between the C-terminus and the G-domain

To better understand the interactions stabilizing specific C-terminus conformations during the MD simulations, pairwise interaction energies between residues of the G-domain and the C-terminus were calculated. These energy values were obtained using CHARMM and represent the sum of non-bonded electrostatic and van der Waals (vdW) contributions.

As a reference point, Figure 13A presents the interaction energy maps from the three independent RanGDP simulations. This map illustrates the pairwise non-bonded interaction energies between residues of the G-domain and the C-terminus. To allow for easier identification of the interacting regions, the final structure of RanGDP from one of the simulations is shown in Figure 13B. In this structural representation, residues are color-coded consistently with the axes of the energy map in Figure 13A, enabling direct correlation between specific structural elements and their corresponding interaction energies.

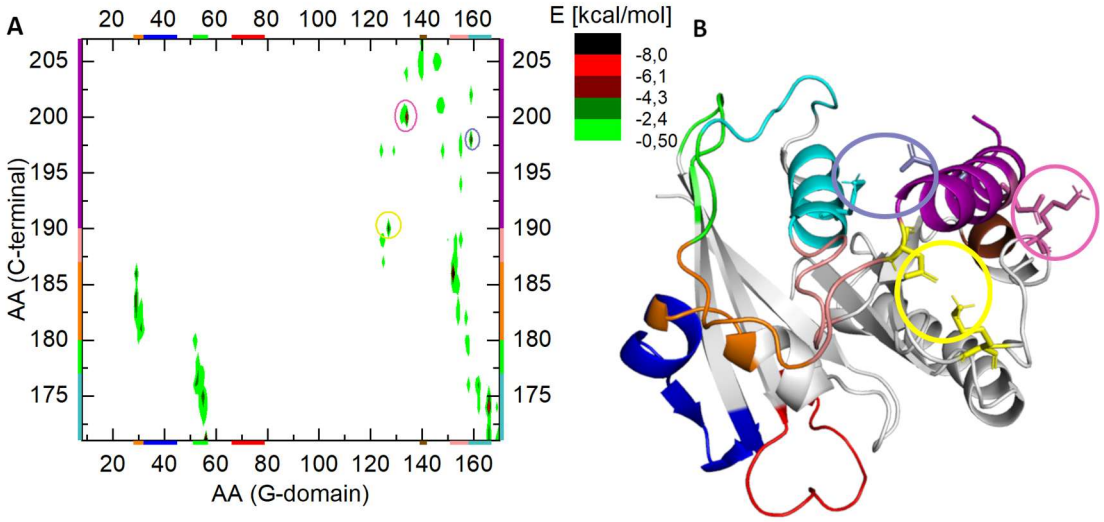

Figure 13. Possible intramolecular interactions during RanGDP simulations. *The interaction energy map between the G-domain and the C-terminus during MD simulation of RanGDP (**A**); 3D structure of RanGDP (**B**). The interacting regions are color-coded along the axes or encircled on the graph and mapped to the 3D structure with identical coloring. The encircled parts of the **A** part highlight the strong ionic interactions of the C-terminal helix, denoted by similar color CPKs on the **B** part of the figure. (69)*

In addition to the well-characterized interaction between the C-terminal tail and the basic patch of the G-domain (residues 139-142, highlighted in brown), our analysis revealed additional elements that contribute to stabilizing the inactive conformation:

- residues 171-180 of the C-terminal loop (denoted in cyan and green) are intercalated between helix α_5 and sheet β_2, where they are stabilized by a combination of hydrogen bonding and electrostatic interactions. Specifically, Leu174 forms a backbone-side chain hydrogen bond with Arg166, while Glu175 interacts with Asn55, Phe176 with His53, and Asp171 with Arg56 through electrostatic and ionic interactions.
- the orange segment of the C-terminal loop (residues 181-186) interacts with helix α_1 (also shown in orange) through two hydrogen bonds: one between Ala181 and Leu31, and another between Ala183 and Arg29. Additionally, the pink segment of the loop (residues 187-189) is positioned in close proximity to the β_6-α_5 loop region, with an ionic interaction observed between Glu186 and Lys152.
- The C-terminal α-helix is anchored to the G-domain through three prominent ionic interactions. The first occurs at its N-terminal end between Asp190 and Lys127 (highlighted in yellow and encircled in yellow CPK representation), the second between Glu198 and Lys159 (highlighted in violet), and the third between Asp200 and Lys134 (highlighted in mauve). Each interaction site is encircled in the corresponding color for clarity.

As the C-terminus adopts distinct orientations relative to the G-domain in each of the three RanGTP MD simulations, the corresponding interaction energy maps are presented separately in Figure 14A, C, and E. These maps reflect the unique interaction patterns observed in each trajectory. The final structures from the respective simulations are shown in Figure 14B, D, and F, providing structural context for the energy profiles.

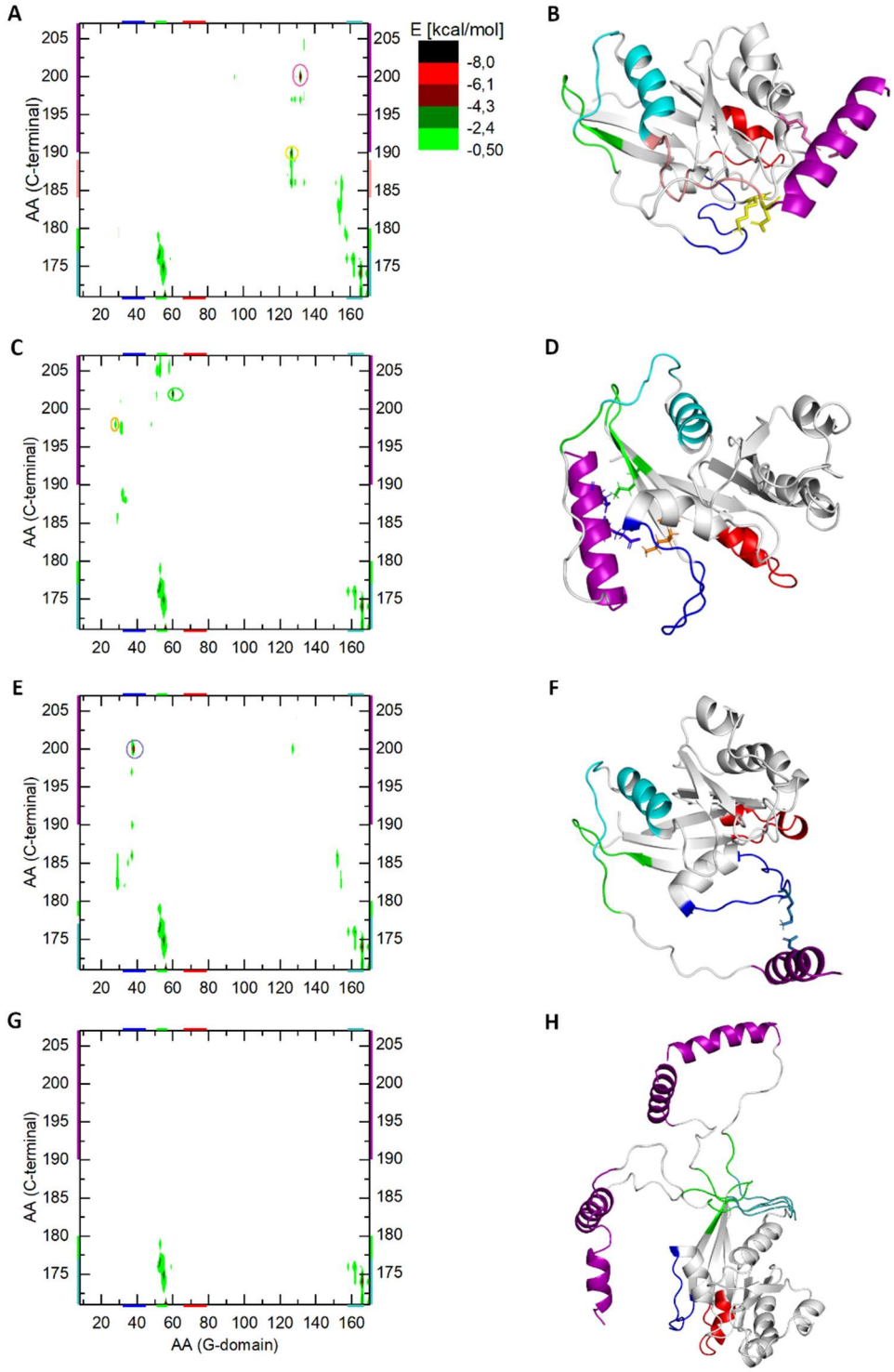

Figure 14. Possible intramolecular interactions during RanGTP simulations. *The interaction energy maps between the G-domain and the C-terminal of RanGTP during the three parallel MD simulation (parts **A**, **C**, **E** of the Figure) and during the MDeNM simulation (part **G** of the Figure). The interacting regions are color-coded both along the axes and encircled on the graph, and the same color scheme is used to map these regions onto the corresponding end structures of each simulation (parts **B**, **D**, **F** and **H** of the Figure). The reported energy values are statistical averages over given MD or MDeNM simulations. (69)*

In all three MD simulations, the N-terminal region of the C-terminus exhibits an interaction pattern similar to that observed in RanGDP, remaining intercalated between helix α_5 and strand β_2 of the G-domain (colored green and cyan).

In the first MD simulation, the C-terminal loop interacts with the β_6-α_5 loop of the G-domain (circled in pink in Figure 14A and colored pink on the structure), while the C-terminal helix is stabilized by two ionic interactions: Asp190 with Lys127 (highlighted in yellow CPK) and Asp200 with Lys132 (highlighted in mauve CPK). In the second simulation, the C-terminal helix attaches to a different region of the G-domain, near β_2 and β_3 (colored green), through ionic interactions between Glu202 and Lys60 (orange CPK), and Glu198 and Lys28 (green CPK). In the third simulation, the C-terminus interacts with switch I via a single ionic interaction between Asp200 and Lys38.

The interaction energy map from the aMDeNM simulation (Figure 14G) reveals that, consistent with all previously analyzed structures, the N-terminal portion of the C-terminal loop (denoted in cyan and green) remains intercalated between helix α_5 and strand β_2 of the G-domain, exhibiting a similar interaction energy profile. No additional interactions are observed in the map, suggesting that the C-terminal helix samples a range of open conformations without binding to the G-domain, as illustrated in Figure 14H, and corroborated by the structural diversity shown in Figure 12E.

4.2. The mechanism of induced switch I opening in RanGTP

4.2.1. Functional significance of the Phe35-GTP-Lys152 triad

During the conformational dynamics study, the *md1* simulation of the parallel MD simulations showed an unusually large conformational change in the switch I region of the structure, transitioning from the closed to an open conformation, which is very similar to that observed in the crystal structure of the RanGDP shown in Figure 15. This conformational change's significance is also shown in the RMSF analysis shown in Figure 10A. As a result of this development, extending the simulations to 1000 ns was necessary.

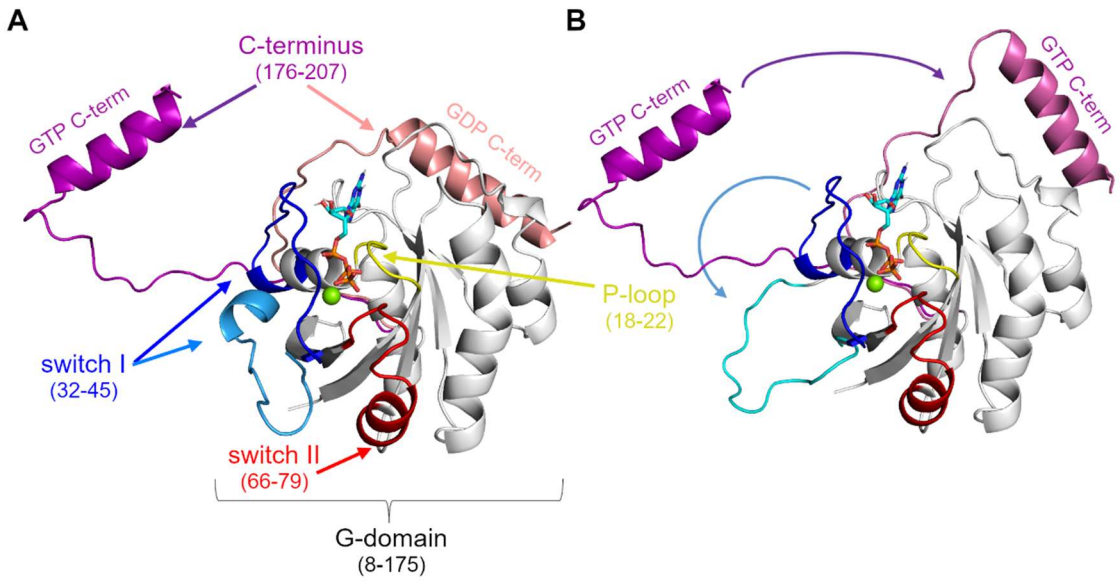

Figure 15. Structural comparison of RanGTP and RanGDP structures. *Full-length structure of RanGTP (5CLL+5CLQ) overlapped to the crystal structure of RanGDP (5CIQ) (**A**). The closed RanGTP switch I conformation is presented in dark blue, while the open RanGDP switch I conformation in light blue; switch II is shown in red. The C-terminus of RanGTP is colored purple, while the C-terminus of RanGDP is pink. The P-loop is yellow, GTP is represented by sticks, while Mg^{2+} by a green sphere. The RanGTP structures from md1 simulation showing open and closed switch I conformations (**B**). (115)*

We calculated and monitored the distances between switch I residues and GTP throughout the simulations to better understand the structural reason for this behavior. Figure 16A shows that during the first 114 ns of the simulation, only two residues, Phe35 and Glu36, maintained continuous contact with GTP. These interactions decreased at approximately 114 ns, corresponding with the opening of switch I. Further underlining the significance of these residues, Figure 16C represents the time evolution of the distances between the COM of the Phe35 aromatic ring and the COM of the guanine moiety of GTP, as well as the distances between the hydrogen-bonding partners Glu36:O and GTP: O2'/O3'. These distances increase steeply while switch I detaches from the G-domain, signaling the change from the closed to open conformation, as illustrated in the inset.

The contrasting case, where switch I remains in the closed conformation (*md2*), is shown in Figure 16B and D. These show that the distance values between the COM of the Phe35 aromatic ring and the COM of the guanine moiety of GTP, as well as the

distance values between the hydrogen-bonding partners Glu36:O and GTP: O2'/O3', show no significant change throughout the simulation time.

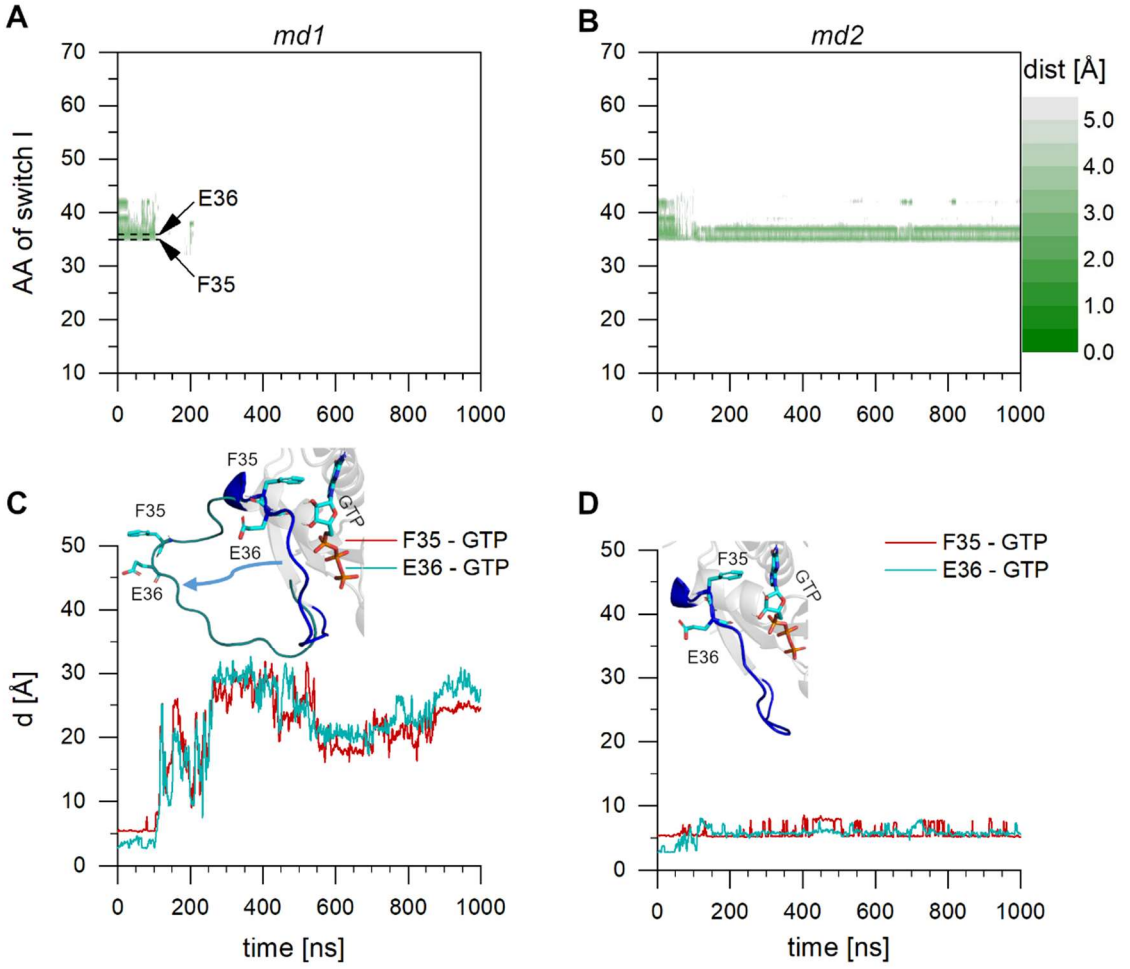

Figure 16. Steric characterization of switch I opening in RanGTP md simulations. *Time dependence of the minimum distances between switch I residues and GTP during md1 (**A**) and md2 simulation (**B**). Distances between the aromatic ring of Phe35$_{COM}$ - the guanine part of GTP$_{COM}$ (red), and between Glu36:O - GTP:O2'/O3' (turquoise) during md1 (**C**) and md2 simulation (**D**). The insets show enlarged views of the RanGTP in md1 and md2 simulations, displaying Phe35, Glu36 and GTP as sticks. (115)*

4.2.2. Structural basis of the triad disruption

To probe further into the reasons behind this behavior and to reproduce the conformational transition between the closed-to-open state of switch I, we performed a series of independent MD simulations, each started from the 103rd ns structure of the md1 trajectory, which is a few ns before the switch I opening initiation, with only their random initial velocity distribution as a difference. Of these seven simulations, only one displayed the mechanism for switch I opening (denoted as *md1'*).

Figure 17A shows the previously identified key inter-residue distances time evolution during the simulations. Firstly, there is an increased value in the distance between the COM of the $Phe35_{ring}$ and the COM of the $GTP_{guanine}$ at ~ 43 ns (red star). Next, the dissociation of Glu36 from GTP happens at ~ 191 ns (turquoise star). Remarkably, switch I remains in the closed conformation, despite these changes. As seen in the structural snapshot of the inset in the Figure, Lys152 stays spatially close to Phe35. In the closed RanGTP structure, the guanine base of GTP maintains an edge-to-face π-π interaction with the aromatic ring of Phe35.

At ~ 210 ns, a significant increase can be observed in the distances between the COM of the Phe35's aromatic ring and the hydrophobic carbon atoms of the Lys152 side chain, signaling the disruption of the triad, which results in the dissociation of switch I from GTP (orange star). Collectively, the analyses of distances shown in Figure 17A implies that the conformational transition from the closed to the open state of switch I is made possible by disrupting both the Phe35-GTP-Lys152 triad and the Glu36-GTP hydrogen bonds.

To determine the reason behind the triad disruption, we performed a detailed analysis of potential perturbations affecting the triad and identified the only plausible mechanism: Figure 17C presents the close approximation of Glu186 towards Lys152 (navy star and structural inset), which leads to a salt bridge formation. This emerging interaction causes the displacement of the hydrophobic side chain of Lys152 from the triad, destabilizing and ultimately breaking it up, triggering the opening of switch I.

Interestingly, the C-terminus position of the RanGTP in the *md1* simulation closely resembled that of the experimentally observed RanGDP (Figure 15A, B), so our next step was to analyze the three parallel simulations of RanGDP for comparison. As shown in Figure 17B, indicated by the high distance values between Phe35 and GDP, switch I stays in the open state throughout all three simulations, exhibiting an opening similar to that seen in *md1'* RanGTP (Figure 17A). In addition, Figure 17D presents that the Lys152-Glu186 interaction is maintained throughout the entire duration of all RanGDP simulations, further underlining its role in stabilizing the open conformation of switch I.

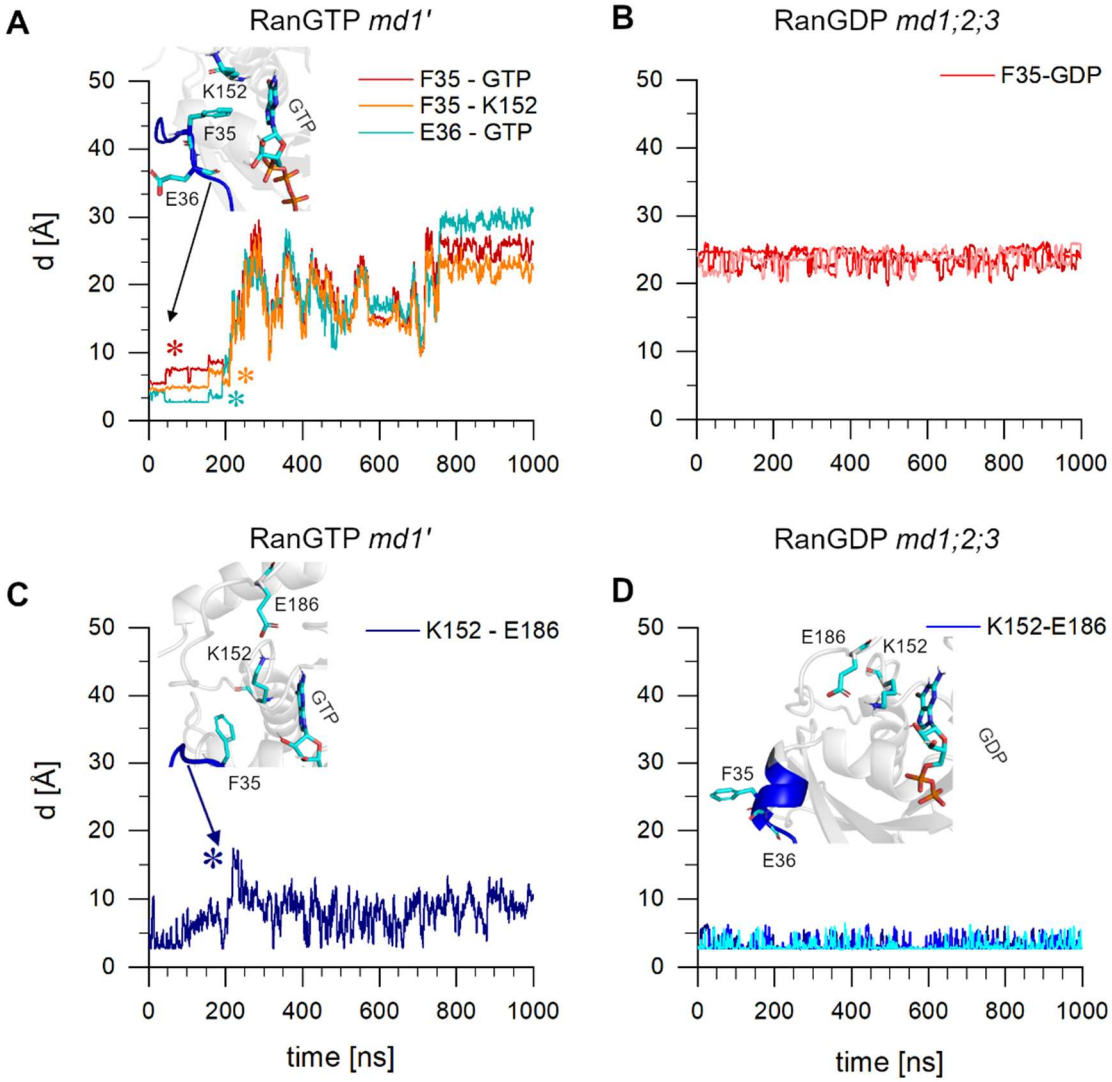

Figure 17. Key switch I - GTP/G-domain interactions involved in switch I opening: *Time dependence of distances between the aromatic ring of Phe35$_{COM}$ - guanine part of GTP$_{COM}$ (red), Glu36:O - GTP: O2'/O3' (turquoise), and the aromatic ring of Phe35$_{COM}$ - hydrophobic carbon sidechain of Lys152$_{COM}$ (orange) during md1' simulation (**A**). Distances between the aromatic ring of Phe35$_{COM}$ - guanine part of GTP$_{COM}$ (shades of red) during three parallel RanGDP md simulations (**B**). Distances between Lys152:NZ-Glu186:OE1/OE2 of RanGTP during md1' simulation and of the three parallel RanGDP simulations (shades of blue), respectively (**C** and **D**). The insets show enlarged views of conformations from the RanGTP and RanGDP simulations. (115)*

The corresponding distance analyses for md' simulations, in which switch I remains in closed conformation, are presented in Figure 18. In every case except one (*md7'*), we observed a transient disruption of Glu36-GTP hydrogen bonds, while the Phe35-GTP-Lys152 triad remains stable. In one case (*md3*), a temporary increase in the Phe35$_{COM}$-GTP$_{COM}$ distance was detected and required further examination.

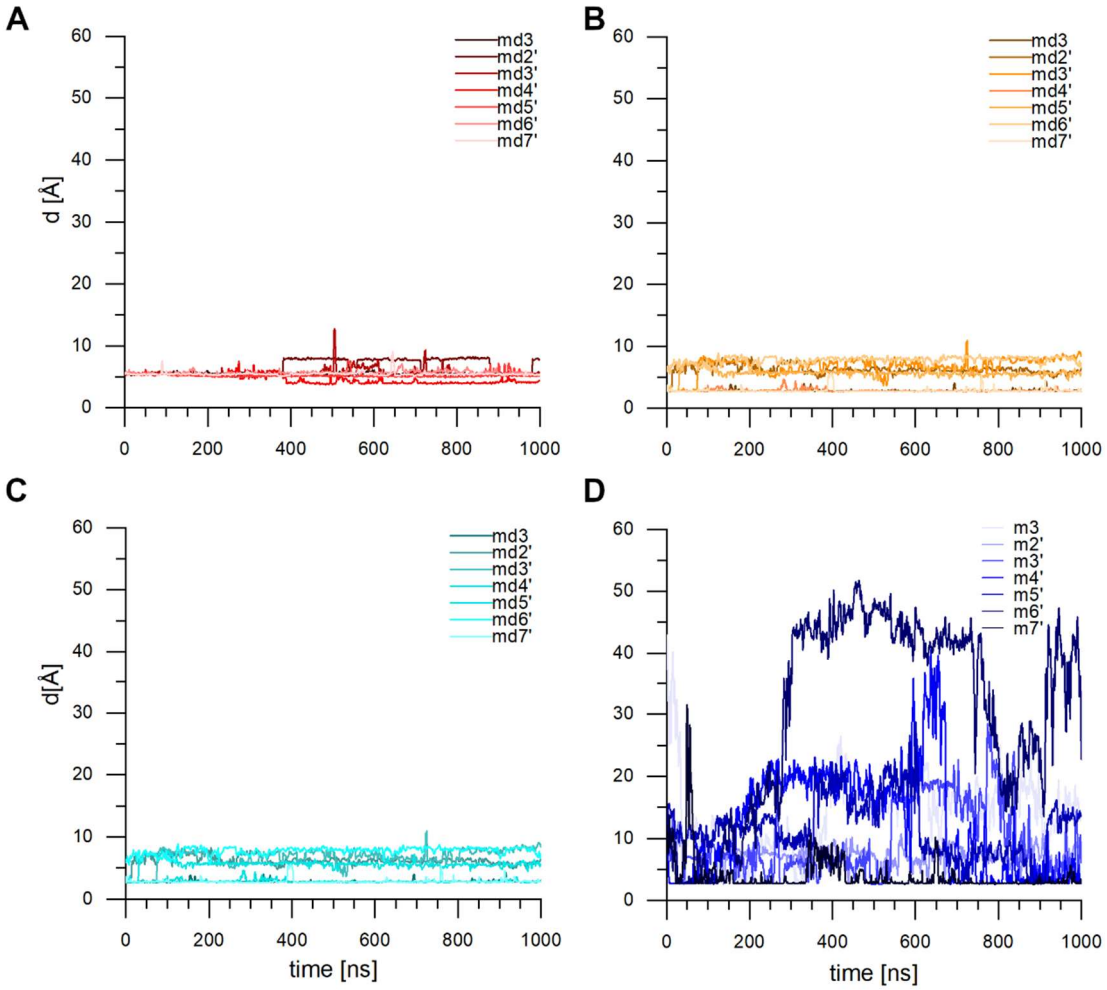

Figure 18. Critical distances during closed simulations: *Time dependence of distances between the aromatic ring of Phe35$_{COM}$ - guanine part of GTP$_{COM}$ (**A**); the aromatic ring of Phe35$_{COM}$ - carbon sidechain of Lys152$_{COM}$ (**B**); Glu36:O - GTP: O2'/O3' (**C**) and Lys152:NZ-Glu186:OE1/OE2 (**D**) during MD simulations in which switch I remained in closed conformation.*

Figure 19 shows the RMSF values of RanGTP md, md' and RanGDP md simulations over 1000 ns simulation time. In Figure 19A, similarly to Figure 10A, *md1* exhibits a large fluctuation of the switch I region compared to the *md2, 3*, or the GDP-bound state. However, its fluctuation in the switch II region is among the smallest, and a similar pattern is observed for the *md1'* simulation relative to the other simulations. These results suggest that the preserved triad stabilizes the closed state of switch I, allowing increased flexibility in the region adjacent to switch II.

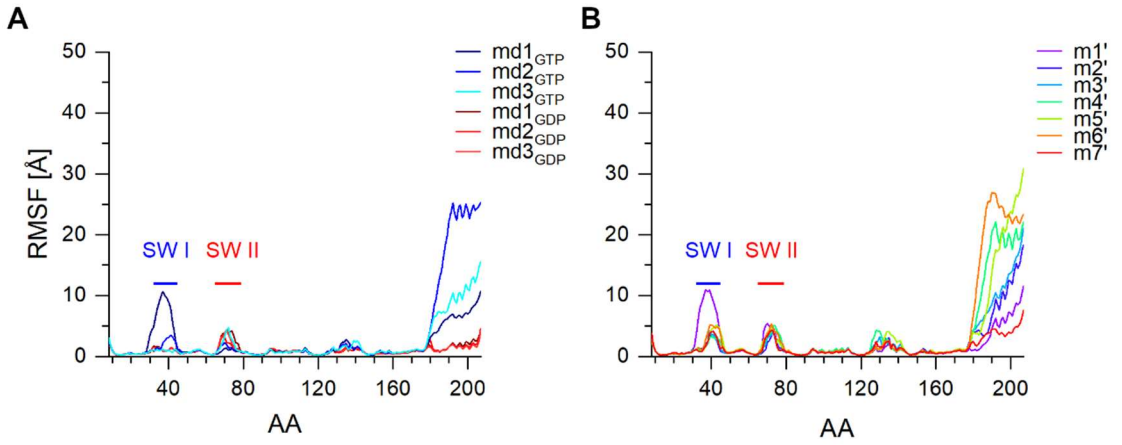

Figure 19. RMSF values during the 1000 ns simulations. *RMS fluctuation values of C_α atoms during RanGTP (shades of blue) and RanGDP (shades of red) md simulations(**A**); and during md' simulations of RanGTP (**B**). (115)*

Shifting the focus to the Lys152-Glu186 interaction as a key factor in the Phe35-GTP-Lys152 triad disruption in one simulation, we next applied a distance constraint to bring Lys152 and Glu186 into close proximity (3.5 Å), starting from a closed switch I conformation of the *md1* simulation (at 20 ns) (Figure 9B). From this starting arrangement, three unconstrained simulations with different velocity distributions were performed (named *md_constr152*). Only one of the three performed simulations showed a closed-to-open switch I conformational transition. As illustrated in Figure 20, the presence of the Lys152-Glu186 interaction disrupts the triad, resulting in the transition of switch I to the open state (Figure 20A). In contrast, when Glu186 moves away from Lys152 upon equilibration, such that the Lys152-Glu186 interaction is absent, switch I remains in the closed conformational state (Figure 20B).

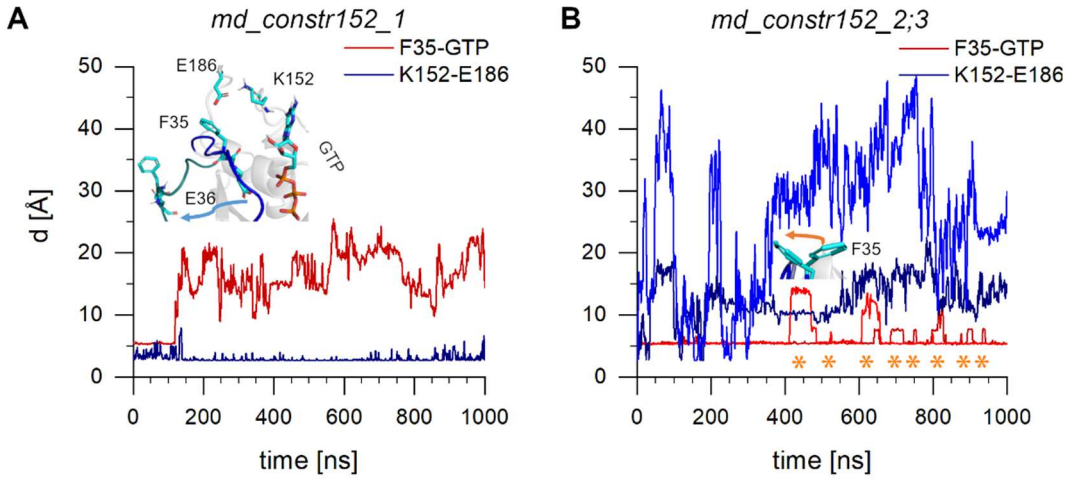

Figure 20. Time evolution of critical distances in constrained MD simulations. *Time dependence of distances between Phe35$_{COM}$ - GTP$_{COM}$ (red) and between Lys152:NZ-Glu186:OE1/OE2 (navy) during md_constr152_1 simulation, where switch I opens (**A**) and md_constr152_2 and _3 simulations, where switch I remains in closed conformation (**B**). The insets show representative enlarged structures, A representing the closed switch I conformation in blue, the open switch I conformation in teal, and B the aromatic ring flipping of Phe35. (115)*

4.2.3. Rearrangement of the Mg^{2+} coordination

In the RanGTP simulations, high RMSF values are observed in the switch I region neighboring switch II (Figure 19). This is an unusual occurrence, as it arises even when the triad remains stable and switch I adopts a conformation similar to that observed in the RanGDP crystal structure, prompting an examination of Mg^{2+} coordination (68). As shown in Figure 21A (open switch I) and Figure 21B (closed switch I), out of 14 RanGTP simulations in 12, the distance value of the Mg^{2+}-Thr42:OG1 interaction exceeds 4 Å, indicating that Thr42 was displaced from the Mg^{2+} coordination sphere.

In Figure 21C an enlarged view of the original Mg^{2+} coordination of the starting crystal structure of RanGTP (PDB 5CLL). It displays the typical octahedral Mg^{2+} coordination with interaction between $Mg^{2+}$and the hydroxyl groups of Thr24 and Thr42, the nonbridging oxygens of the γ- and β-phosphates of GTP, and two water molecules (103). The observed loss of the Thr42-Mg^{2+} interaction is a known step in the nucleocytoplasmic transport cycle and is not expected to occur spontaneously (128).

In the case of the two outlier simulations, where the average of the Mg^{2+}-Thr42 distance remained below 4 Å (*md3, md_constr152_3*), Thr42 stayed in the coordination sphere, hence stabilizing the switch I region in proximity to switch II in a closed

conformation. The octahedral coordination is regained through the interaction between the Asp65:OD1 and Mg^{2+}, by replacing a water molecule that had been displaced from the coordination sphere. Therefore, the observed loss of the Thr42-Mg^{2+} interaction in both the open (where both the triad and the Thr42-Mg^{2+} interaction are disrupted; Figure 21A) and partially closed (where the triad remains stable but the Thr42-Mg^{2+} interaction is broken; Figure 21B) switch I conformations shows that disruption of the Phe35-GTP-Lys152 triad is a key factor for the closed-to-open transition of switch I, similar to that of RanGDP.

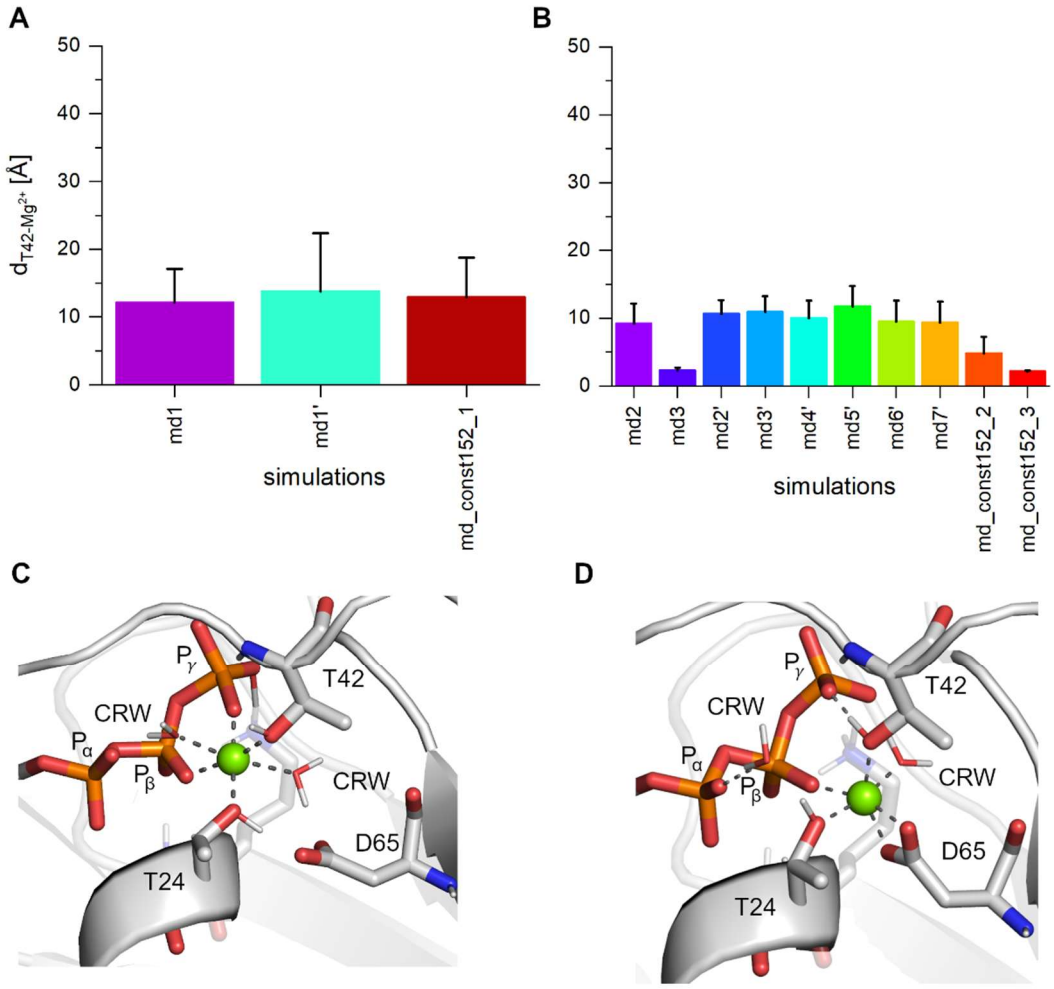

Figure 21. The loss of Thr42-Mg^{2+} coordination. *Average distance between Thr42:OG1 - Mg^{2+} during the simulations with switch I in the open (**A**) or closed conformation (**B**). The octahedral Mg^{2+} coordination in the crystal structure of RanGDP-BeF-RanBD1 (PDB 5CLL) (**C**); the loss of the octahedral Mg^{2+} coordination in the energy minimized structure after gradually decreasing the harmonic restraints on the heavy atoms during energy minimization (**D**). (115)*

4.2.4. Inducing the fully open conformation of switch I

To test our hypothesis whether the disruption of the Phe35-GTP-Lys152 triad alone is enough to drive a complete switch I transition to the open state, a new set of MD simulations was performed by taking an energy-minimized structure where heavy-atom restraints preserved the octahedral coordination of Mg^{2+}. In the next step, an upper-wall distance restraint (≤ 4 Å) was applied between Lys152 and Glu186 to promote interaction, which could facilitate the triad disruption during the simulation dynamics.

Figure 22A shows the Phe35-GTP distances, where the Phe35-GTP-Lys152 triad was disrupted in all simulations, resulting in Phe35 being displaced away from GTP. On the other hand, Mg^{2+} stays in its original coordination state throughout the 1 μs-long simulations, as can be observed in Figure 22C. Thus, switch I undergoes a conformational change to a partially open state on the side of the disrupted triad, as illustrated in the inset. This indicates that triad disruption alone is insufficient to fully drive switch I into the open conformation observed in the RanGDP crystal structure.

To replicate the behavior, we used the final structure of the previous simulations and gradually increased the distance between Mg^{2+} and Thr42 to 10 Å. This value is used to simulate the effect of a GAP during the GTP hydrolysis (48). We performed 5 parallel, unconstrained MD simulations. As shown in panels B and D of Figure 22, both previously used distance measures increase, demonstrating that the transition to the fully open state of switch I conformation is occurring, as further illustrated in the inset of Figure 22D.

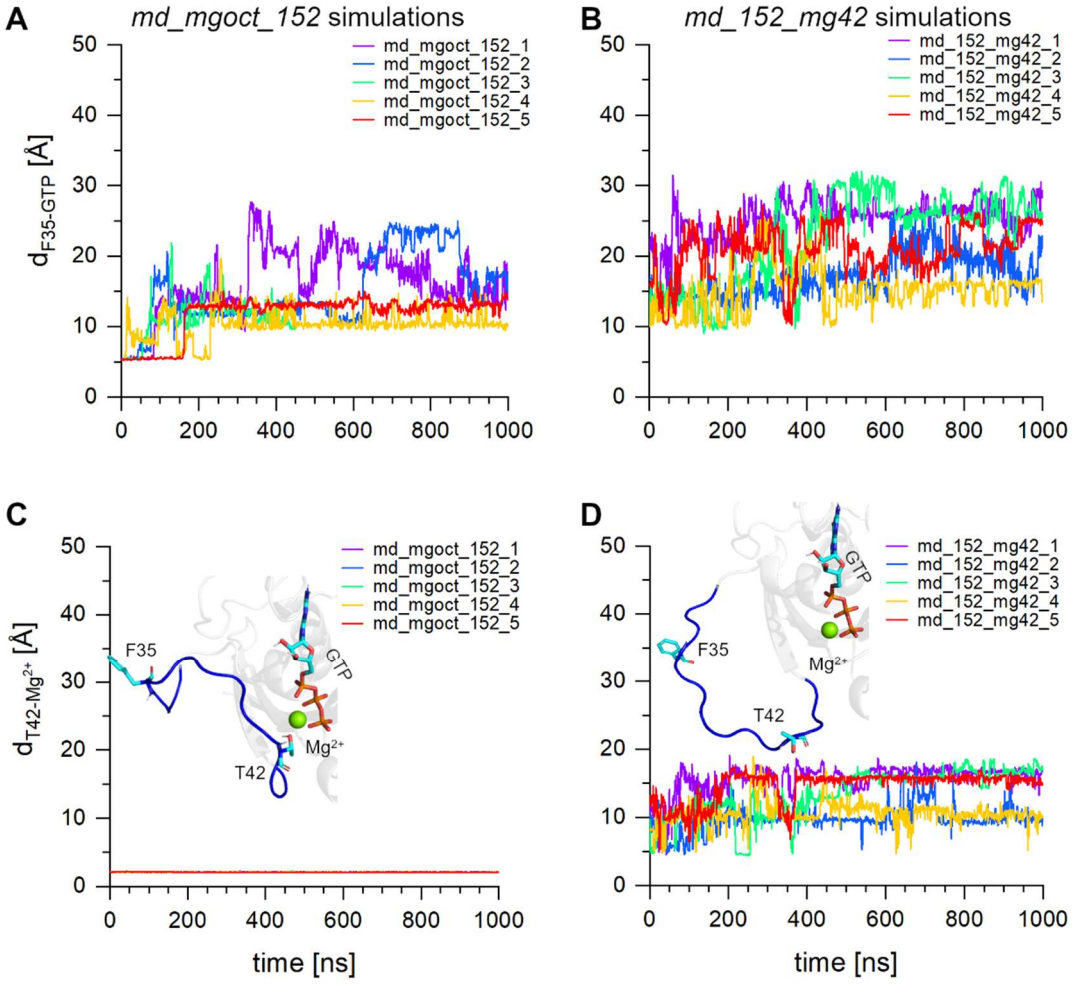

Figure 22. Sequential disruption of the Phe35-GTP-Lys152 triad and Thr42-Mg^{2+} leading to switch I opening. *Time evolution of distances $Phe35_{COM}$ - GTP_{COM} (**A**) and between Thr42:OG1-Mg^{2+} (**C**) during md simulations starting from energy-minimized structures subjected to harmonic restraints, followed by the application of an 'upper wall constrain' between Lys152 - Glu186. (**B**) and (**D**) show the same distances after gradually removing Thr42 from Mg^{2+} to 10 Å. The insets of (**C**) and (**D**) show enlarged structural views of the 'partially opened' and the 'fully' opened RanGTP during simulation. (115)*

5. DISCUSSION

5.1. The nucleotide-specific functional movement of the C-terminus

5.1.1. Evaluating conformational dynamics using various simulation techniques

Previous molecular dynamics studies have demonstrated the utility of MD simulations in characterizing the conformational flexibility of key functional regions, including switch I and switch II, across members of the Ras superfamily (117, 129-133). Accordingly, and in light of prior experimental evidence, we anticipated that the C-terminal region of Ran would display increased flexibility in its GTP-bound state relative to the GDP-bound form, reflecting a more dynamic conformational behavior. The results shown in Figure 10A support this expectation: the C-terminus in the GTP-bound simulations exhibits significantly greater fluctuations, with the minimum fluctuation value nearly twice as high as that observed in the GDP-bound simulations. As noted previously, in contrast to the behavior reported for K-Ras, the switch I region in RanGTP also shows slightly elevated fluctuation levels compared to RanGDP. This behavior may be attributed to a conformational transition of switch I from a structurally ordered open state (α-helix followed by a β-turn; Figure 4A) to a more disordered, loop-like closed state in the GTP-bound form (Figure 4B). By contrast, the switch II region behaves as expected, becoming more rigid upon GDP-to-GTP exchange. Collectively, these observations highlight distinct features of Ran's conformational dynamics within the Ras superfamily and may reflect its specialized role in nuclear transport.

By applying the aMDeNM method, we were able to explore a broader conformational space of RanGTP, as evidenced by the increased fluctuations of the C-terminus compared to those observed in conventional MD simulations (Figure 10B). However, this outcome is partially influenced by a methodological limitation: the introduction of bias through the selection of normal modes specifically targeting C-terminal motions. Consequently, fluctuations in the switch I region are not captured in the aMDeNM results.

In this study, we focused specifically on the movement of the C-terminal region of RanGTP, as no complete experimental structure of this form currently exists. To our

knowledge, this work represents the first detailed computational characterization of the C-terminal dynamics in RanGTP.

To validate the coordinate transformation approach used for C-terminus visualization, we examined the results obtained for RanGDP (Figure 11), which aligned well with expectations and exhibited minimal conformational variability, as reflected by the limited range mapped in the analyzed plane.

The three RanGTP MD simulation trajectories identify distinct local minima during the conformational mapping of the C-terminal region, with simulations 1 and 2 sampling more confined conformational spaces (Figure 12B and C), while simulation 3 explores a broader and more extensive range of motions (Figure 12D). Notably, all mapped conformations cluster predominantly on the same side of the G-domain, near the switch regions. In contrast, due to the targeted selection of normal modes, the aMDeNM results map a wide range of open conformations on different sides of the G-domain (Figure 12E).

The limited number of crystal structures that include the C-terminus of RanGTP are all determined in complex with Ran-binding proteins, where the C-terminal helix consistently binds by embracing the Ran-binding domain. As a result, these experimental structures show the C-terminus in similar, constrained conformations. Complementary to this, the aMDeNM simulation results demonstrate that the C-terminus of RanGTP can sample a wide conformational space, enabling it to interact flexibly before adopting a stabilized three-dimensional structure upon binding to Ran-binding domains.

5.1.2. Structural impact of C-terminus and G-domain interactions

Our analysis revealed stabilizing interactions within the RanGDP structure that maintain the C-terminus in its inactive conformation. Beginning at the N-terminal end of the C-terminal region, we identified stabilizing contacts between residues 171-180 and the interface formed by the α_5 helix and β_2 sheet (Figure 23). Further interactions occur between residues 181-186 and the α_1 helix, as well as the loop region connecting β_6 and α_5. Finally, the N-terminal end of the C-terminal helix is anchored by three strong ionic interactions with the G-domain. These interactions include a mixture of backbone-to-sidechain hydrogen bonds, electrostatic interactions, and strong ionic bonds. Collectively, these interactions appear to play a crucial role in securing the C-terminus in its inactive

position, underscoring the complexity of intramolecular contacts that regulate RanGDP's structural stability.

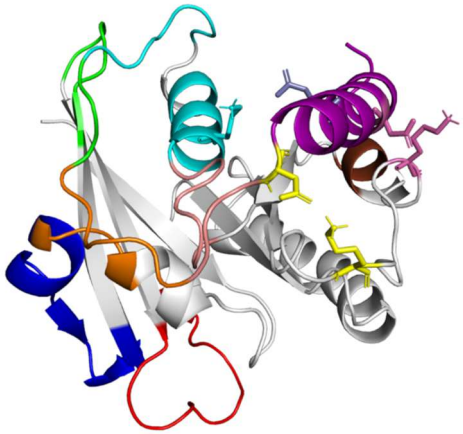

Figure 23. The 3D structure of RanGDP. *All interacting regions are mapped onto the structure using the same coloring as in Figure 13, and the strong ionic interactions of the C-terminal helix are highlighted with identically colored CPK representations.*

Since the three MD simulations of RanGTP concluded with the C-terminus positioned at different regions of the G-domain, we discuss each simulation separately (Figure 24A-C). However, a common feature across all simulations is the persistence of the interaction between the N-terminal segment of the C-terminus and the interface between the α_5 helix and β_2 sheet of the G-domain. This consistent intercalation suggests that the N-terminal portion of the C-terminus remains anchored in this region regardless of the distal conformational variability. This observation provides a strong indication of why, in many RanGTP crystal structures, large portions of the C-terminal region are unresolved, with disorder typically beginning around residue 176 and extending up to residue 183. The inherent flexibility and lack of stable contacts beyond this anchoring point likely contribute to the difficulty in resolving these segments crystallographically.

In the first MD simulation (Figure 24A), the C-terminal loop primarily interacts with the β_6-α_5 loop of the G-domain. This interaction appears to be reinforced by ionic bonds that stabilize the adjacent C-terminal helix. The second simulation (Figure 24B) presents a different interaction pattern, wherein the C-terminal helix shifts its binding site to a region near the β_2 and β_3 strands of the G-domain with an ionic interaction. In the third MD simulation (Figure 24C), the C-terminus gets attached to switch I *via* an ionic interaction. In the third MD simulation, we observed the C-terminus engaging directly with switch I through ionic interactions. The switch I region is known to undergo

conformational changes upon nucleotide binding and hydrolysis, playing a key role in Ran's activation mechanism.

Collectively, these simulations highlight the versatility and complexity of C-terminal interactions with the G-domain, which involve multiple binding partners and ionic contacts.

Understanding the interactions described above allows us to interpret the distinct RMSF behavior observed for switch I across the three simulations (Figure 10A). Notably, the RMSF of switch I is reduced in the third simulation compared to the first two. This decrease in flexibility indicates that the ionic interaction formed between the C-terminus and switch I effectively restricts the mobility of switch I, confining it to a more stable and defined conformational state. However, it remains to be determined whether the stabilized interaction corresponds to a biologically relevant state. In contrast, during the first and second simulations, where such direct ionic tethering is absent, switch I exhibits greater flexibility and samples a broader range of conformations.

During the aMDeNM simulations (Figure 24D), the only persistent interaction observed is the intercalation of the N-terminal end of the C-terminal region between the α_5 helix and the β_2 sheet of the G-domain. Apart from this stable contact, no additional interactions involving the C-terminal helix are maintained, suggesting that the C-terminal helix adopts a variety of more open and flexible conformations throughout the simulation.

By comparing the C-terminus conformations sampled by different simulation methods to the available X-ray structures of Ran complexes, several notable observations emerge. In two of the three conventional MD simulations, the final C-terminal conformations closely overlap with the region corresponding to the RanBP binding site on the G-domain. Given that the starting structure for these RanGTP simulations was derived from the RanBP1 complex, this overlap underscores the constrained conformational sampling inherent to standard MD approaches, which tend to remain close to the initial, biologically relevant binding modes.

Conversely, the third MD simulation yields a C-terminus conformation that does not coincide with any known biologically relevant surfaces of the G-domain, suggesting a potentially non-physiological or transient state.

In contrast, the aMDeNM simulations reveal that the C-terminus explores a broad ensemble of open conformations that do not engage with the G-domain. These more flexible and extended states may be crucial for enabling the C-terminus to interact with molecular partners such as RanBPs during the cellular cycle. The greater conformational diversity captured by aMDeNM highlights its advantage in sampling rare but functionally important conformations that standard MD simulations might overlook.

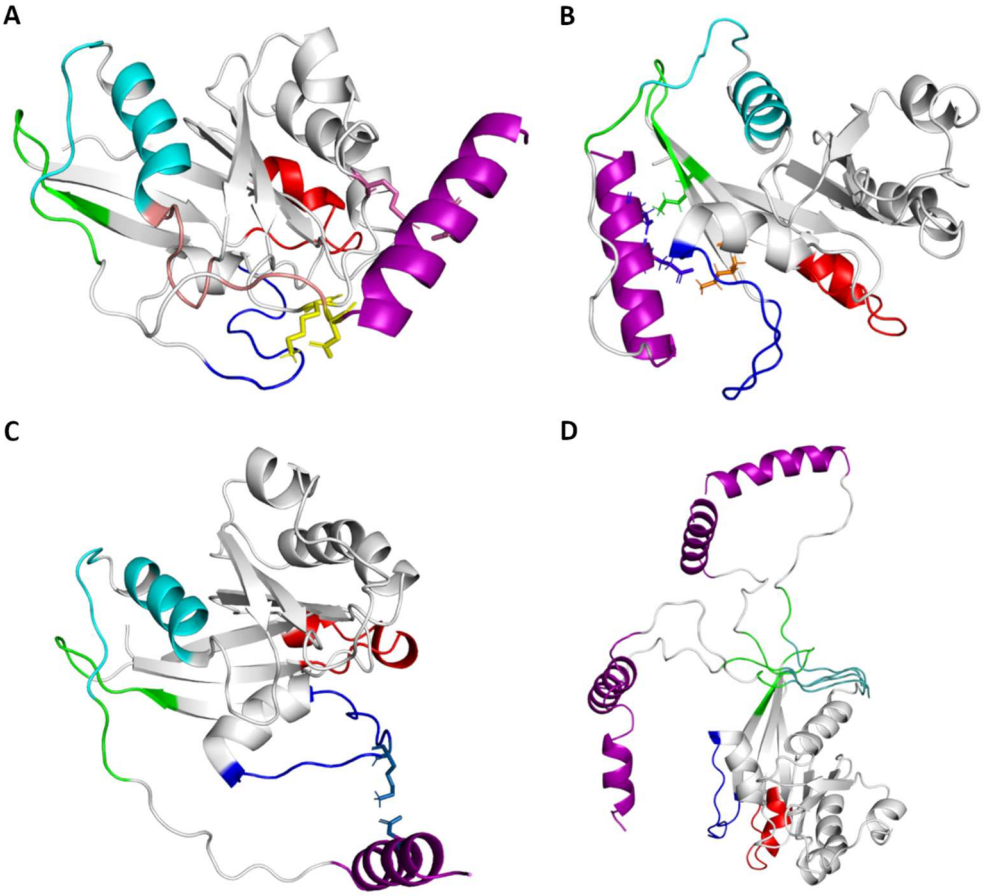

Figure 24. The 3D structure of RanGTP obtained from both simulation methods. *Final structures from three MD simulations after 200 ns are shown in panels A–C, and three representative end structures from aMDeNM simulations are shown in panel D. Interacting regions are mapped using the same color scheme as in Figure 14, and strong ionic interactions of the C-terminal helix are highlighted with correspondingly colored CPK representations.*

5.2. Key interactions of RanGTP involved in triggering the conformational change of switch I

5.2.1. Mapping the structural background of the switch I opening

In one of the RanGTP MD simulations switch I underwent a conformational change that led to an open-like structure resembling that of RanGDP (Figure 15). To better

understand and quantify this conformational shift, we analyzed key interactions that could correlate with the degree of "openness" (Figure 16). Two potentially significant interactions emerged: one between Phe35 and GTP, and another involving Glu36 and the GTP molecule (inset in Figure 16C).

To further investigate this mechanism, we conducted an additional set of independent MD simulations. In one of these, we observed an alternative mode of switch I behavior: despite the dissociation of both the Phe35-GTP and Glu36-GTP interactions, switch I remained in a closed conformation (Figure 17). This finding suggests that the disruption of these two interactions alone is insufficient to drive the conformational transition. Instead, an additional stabilizing interaction must also be lost to allow the switch to open.

As shown in the structural snapshot (Figure 17A), Lys152 is positioned in close spatial proximity to Phe35 in the closed RanGTP conformation. In this state, the guanine base of GTP forms an edge-to-face π-π interaction with the aromatic ring of Phe35. This is complemented by hydrophobic contacts between Phe35 and the aliphatic segment of the Lys152 side chain, together establishing a stabilizing triad composed of Phe35, GTP, and Lys152. This triad appears to be crucial for maintaining switch I in its closed, active conformation. Additionally, hydrogen bonds between Glu36 and the phosphate groups of GTP provide further stabilization to this interaction network. It seems that their collective disruption is necessary for the transition toward an open, GDP-like conformation.

The perturbation responsible for the disruption of this triad arises from the approach of Glu186 toward Lys152, which results in the formation of a salt bridge between the two residues. This new electrostatic interaction effectively displaces the hydrophobic side chain of Lys152 from its position within the Phe35-GTP-Lys152 triad, thereby destabilizing and ultimately dismantling the interaction network. The breakdown of this stabilizing triad appears to act as a trigger for the conformational opening of switch I.

Figure 25 provides a structural overview of the conformational transition of RanGTP from the closed to the open state, as observed in our simulations. In the closed conformation (Figure 25A), switch I is stabilized by a hydrophobic triad formed by Phe35, GTP, and Lys152, in addition to hydrogen bonds between Glu36 and GTP. These

interactions maintain the integrity of switch I and anchor it to the G-domain. As the transition progresses, an intermediate state emerges (Figure 25B), characterized by the formation of a salt bridge between Glu186 and Lys152. This new interaction displaces the Lys152 side chain from the triad, leading to the reorientation of the Phe35 aromatic ring away from GTP and the concurrent disruption of the Glu36-GTP hydrogen bonds. These changes collectively destabilize switch I. In the final open state (Figure 25C), switch I is fully detached from the G-domain, resembling the conformation typically seen in RanGDP.

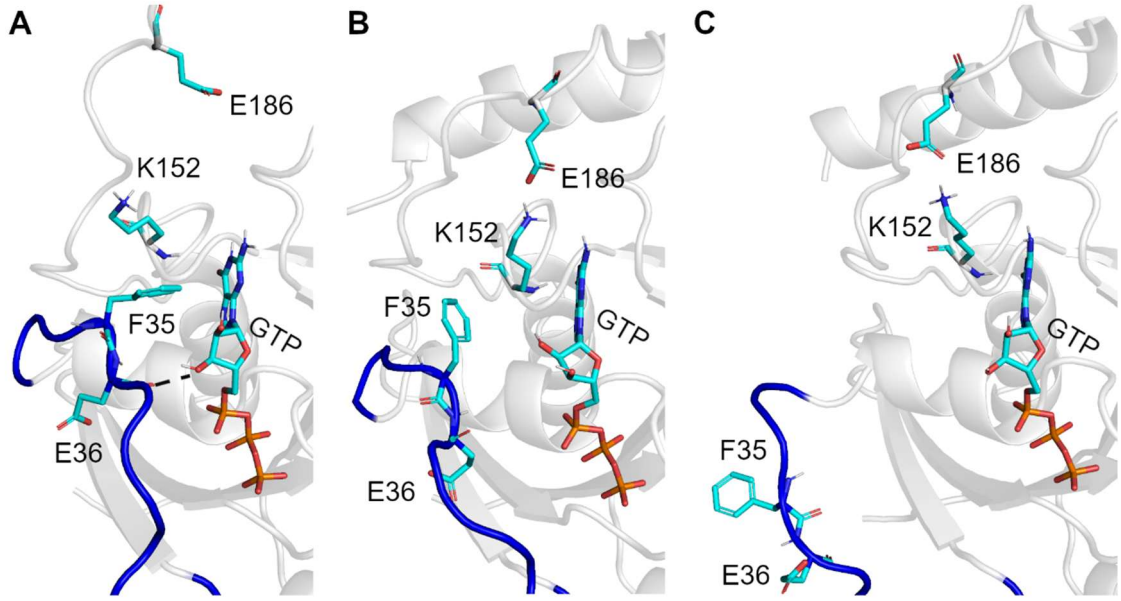

Figure 25. Disruption of the Phe35-GTP-Lys152 triad that drives switch I opening. *The stable triad with the closed switch I conformation; the Glu36-GTP H-bond is marked with a black dashed line (**A**). The intermediate structure showing the broken triad and Lys152-Glu186 interaction (**B**). The open switch I conformation (**C**). (115)*

A recurring behavior was observed in both simulations, where switch I remained in the closed conformation (can be observed in Figure 18A and indicated by orange stars in Figure 20B): the aromatic ring of Phe35 undergoes transient displacements from GTP. As shown in the inset of Figure 20B, these events correspond to ring-flipping motions of the Phe35 side chain (134-136). Despite these temporary displacements, the hydrogen bonds between Glu36 and GTP persist, continuing to stabilize switch I in its closed state. Moreover, following each aromatic ring flip, the contact between Lys152 and GTP is maintained, allowing the Phe35-Lys152-GTP triad to re-form. This dynamic reassembly of the triad appears sufficient to preserve the closed conformation of switch I, highlighting

the robustness of the interaction network that maintains the active state of RanGTP despite transient local fluctuations.

In rare instances—such as observed in the original *md1* simulation (Figure 16A, C)—the flipping of the Phe35 aromatic ring occurs in a conformation of switch I, where the stabilizing hydrogen bonds between Glu36 and GTP are already disrupted. Under these conditions, the Phe35 flip leads to the breakdown of the Phe35-GTP-Lys152 triad without requiring any perturbation of Lys152 itself. This isolated disruption is sufficient to destabilize switch I, ultimately triggering its transition into the open conformation.

5.2.2. The significance of the disruption in the Mg coordination sphere

In RanGTP simulations, we noticed elevated RMSF values specifically in the switch I region near switch II, even in cases where the triad appeared stable. This observation prompted us to examine more closely how Mg^{2+} coordination (6, 103, 137) changed throughout the simulation setup. Following energy minimization, we found an unexpected rearrangement: the negatively charged Asp65 moved into the Mg^{2+} coordination sphere, displacing both the γ-phosphate and one of the coordinating water molecules (Figure 21D). This shift was accompanied by a new hydrogen bond forming between the γ-phosphate and Thr42, while the displaced water molecule moved closer to the α-phosphate and formed a hydrogen bond there. During the early stages of the subsequent dynamics, the γ-phosphate regained its coordination with Mg^{2+}; however, the displaced water molecule did not return to the literature-described, distance-based coordination sphere, and Asp65 remained firmly bound. This led to Mg^{2+} adopting a transient hepta-coordinated state, which departs from its preferred symmetric octahedral geometry and likely contributes to the observed local instability (137). Over time, this distortion appears to be alleviated as Thr42 leaves the coordination sphere, resulting in a partial opening of switch I. This sequence of events suggests a dynamic interplay in the coordination environment around Mg^{2+} that may underlie the structural fluctuations observed in switch I.

In the two simulations where the Mg^{2+}-Thr42 distance stayed consistently below 4 Å (md3 and md_constr152_3), Mg^{2+} maintained its coordination with Thr42. This interaction appeared to stabilize the switch I region near switch II, keeping it in a closed conformation. Additionally, Mg^{2+} restored its preferred octahedral coordination geometry

by forming a bond with Asp65:OD1, effectively replacing a water molecule that had been displaced from the coordination sphere.

5.2.3. The induction of full switch I opening

Collectively, the loss of the Thr42 - Mg^{2+} interaction, which we observed in both fully open (Figure 21A) and partially closed (Figure 21B) switch I conformations, highlights the disruption of the Phe35-GTP-Lys152 triad as a critical step for switch I to adopt a fully open conformation, similar to what is seen in RanGDP. To explore this further, we refined our methodology to test whether disruption of this triad alone was sufficient to trigger the full switch I transition. After performing simulations under these conditions, we found that Mg^{2+} coordination remained stable, and the switch I region only shifted to a partially open state. Subsequently, by gradually increasing the Thr42-Mg^{2+} distance in another set of simulations, we observed that switch I consistently adopted a fully open conformation. Mutational experiments support the importance of these interactions, as substitutions at these sites weaken binding to effectors such as RanBP1 and RanGAP1 (128, 138, 139).

In summary, our findings show that disruption of Mg^{2+} coordination alone induces only a partial opening of switch I. This half-open conformation is consistent with experimentally determined RasGTP structures (11, 140-143) and corresponds to the so-called **state 1** conformation, which represents an open, effector-nonbinding state, in contrast to **state 2**, the closed, effector-binding conformation. Both states are observed in our simulations, as summarized in Figure 21B. In eight of the ten trajectories, switch I adopts a state 1 conformation consistent with the partially open structure described above, whereas in two trajectories switch I remains in the closed, state 2 conformation.

A complete transition to the fully open switch I conformation, as observed in RanGDP, requires the coordinated disruption of both Mg^{2+} coordination and the Phe35-GTP-Lys152 triad. While loss of Mg^{2+} coordination can be induced by GAP activity, disruption of the triad in our simulations is driven by reorientation of Lys152 toward Glu186, resulting in formation of a stabilizing Lys152-Glu186 salt bridge.

Compared with Ran, Ras differs markedly. The residue corresponding to Glu186 is located within the HVR region and is absent in experimentally determined Ras structures, meaning that the Ras triad is not destabilized from the side of the Lys147

(equivalent to Lys152 in Ran). Consequently, a binding partner is necessary to achieve the fully open conformation. Multiple structural studies have demonstrated that, in the nucleotide-free state, switch I of Ras adopts a fully open conformation when bound to SOS (one of Ras's GEF proteins) (144-146); understandably so, since the triad does not exist in the absence of the nucleotide. From the other side, concerning the critical role of Mg^{2+} coordination, in silico studies, alongside experimentally determined structures (142, 143, 147-149), have proposed partially open intermediate conformations to describe the mechanism of nucleotide release during Ras GDP-to-GTP exchange. (150-153).

Because spontaneous opening of switch I is rare, the mechanism by which Ran binding partners promote this transition remains an important question. On one hand, loss of the Thr42-Mg^{2+} interaction is a well-established GAP-induced effect (48, 103, 128). On the other hand, X-ray structures of Ran in complex with RanBP1 (48) and with the Ran-binding domains of RanBP2 (32, 46, 103) reveal direct contacts with Phe35, indicating that effector binding can modulate triad stability. In addition, Lys152 has been identified as an in vivo SUMOylation site (154, 155), and the SUMO-E3 ligase region of RanBP2 interacts with Ran in the vicinity of this residue. Together, these interactions provide plausible mechanisms for triad destabilization and suggest that partner binding or post-translational modification may create the conditions necessary to induce the switch I opening mechanism described in this study.

The switch I opening observed in our study may reflect a general principle for other family members of small GTPases, where the triad destabilization and the loss of Thr-Mg^{2+} interaction may promote conformational on-to-off transitions. Based on this, two potential directions emerge from the present study. First, the switch I opening mechanism could be investigated across other small GTPases to assess whether it represents a generalizable feature within the family. Second, this framework may help identify potential regulatory or druggable sites by focusing on inducing the inactive switch I conformation.

6. CONCLUSION

A. By employing different simulation approaches (MD and aMDeNM), we were able to characterize the nucleotide-dependent dynamical behavior of the C-terminal end of Ran, the biological role of which has been extensively reported in numerous experimental studies.

- In the inactive GDP-bound form, the C-terminus end stays rigidly attached to the G-domain, auto-inhibiting the effector binding site. Besides the interactions known in the literature, we identified three intense ionic interactions that keep the C-terminal helix rigidly bound to the G-domain, namely, Asp190/Lys127, 198Glu/159Lys, and 200Asp/134Lys.
- In the active GTP-bound form, we achieved extensive mapping of C-terminal conformations, which allowed us to envisage how RanGTP interacts with its macromolecular partners.

B. We defined the mechanism underlying switch I opening in RanGTP, demonstrating that full transition to the open switch I conformation requires two perturbations:

(i) disruption of the Phe35-GTP-Lys152 triad, initiated by the reorientation of Lys152 through interaction with Glu186, and

(ii) the displacement of Thr42 from the Mg^{2+} coordination sphere. These changes, in turn, also destabilize the hydrogen bonds between Glu36 and GTP, enabling switch I to transition into an open conformation that resembles the inactive state of RanGDP.

Together, these findings define a new mechanistic basis for the switch I 'on' - to 'off' transition and point to potential therapeutic strategies for modulating small GTPases in cases where pathogenic mutations stabilize the active state.

7. SUMMARY

Molecular dynamics (MD) simulations offer an effective approach to study the conformational dynamics of small GTPases. In the present work, we investigated the nucleotide-dependent conformational dynamics of Ran, with a particular focus on the C-terminal region and the molecular mechanism underlying switch I opening by MD and aMDeNM simulations. Our results reveal pronounced nucleotide-dependent differences in Ran dynamics. In the GTP-bound state, the C-terminus exhibits substantially higher flexibility than in the GDP-bound form. These features suggest that Ran requires enhanced conformational plasticity in its active state, consistent with its role in nucleocytoplasmic transport.

Across all simulations, a conserved anchoring interaction between the N-terminal segment of the C-terminus and the α_5-β_2 interface of the G-domain was identified, providing a structural explanation for the frequent disorder of distal C-terminal residues in RanGTP crystal structures.

In addition, this study elucidates the molecular basis of switch I opening in RanGTP. Disruption of Mg^{2+} coordination alone induces only a partially open switch I conformation corresponding to the state 1 conformation described for Ras proteins, an open, effector-nonbinding state. A full transition to the RanGDP-like, fully open switch I conformation requires coordinated disruption of both Mg^{2+} coordination and the Phe35-GTP-Lys152 stabilizing triad. Triad destabilization is initiated by reorientation of Lys152 toward Glu186, leading to formation of a Lys152-Glu186 salt bridge. Together, these findings define a two-step mechanism for switch I opening and provide a framework for understanding Ran's unique conformational regulation.

8. REFERENCES

1. Joseph J. Ran at a glance. Journal of Cell Science. 2006;119(17):3481-4.

2. Boudhraa Z, Carmona E, Provencher D, Mes-Masson AM. Ran GTPase: A Key Player in Tumor Progression and Metastasis. Front Cell Dev Biol. 2020;8.

3. Matchett KB, McFarlane S, Hamilton SE, Eltuhamy YSA, Davidson MA, Murray JT, et al. Ran GTPase in Nuclear Envelope Formation and Cancer Metastasis. Cancer Biology and the Nuclear Envelope: Recent Advances May Elucidate Past Paradoxes. 2014;773:323-51.

4. Haggag YA, Matchett KB, Dakir E, Buchanan P, Osman MA, Elgizawy SA, et al. Nano-encapsulation of a novel anti-Ran-GTPase peptide for blockade of regulator of chromosome condensation 1 (RCC1) function in MDA-MB-231 breast cancer cells. Int J Pharmaceut. 2017;521(1-2):40-53.

5. Cavazza T, Vernos I. The RanGTP Pathway: From Nucleo-Cytoplasmic Transport to Spindle Assembly and Beyond. 2016;Volume 3 - 2015.

6. Bourne HR, Sanders DA, McCormick F. The GTPase superfamily: conserved structure and molecular mechanism. Nature. 1991;349(6305):117-27.

7. Hilgenfeld R. How do the GTPases really work? Nat Struct Biol. 1995;2(1):3-6.

8. Vetter IR, Wittinghofer A. The guanine nucleotide-binding switch in three dimensions. Science. 2001;294(5545):1299-304.

9. Wennerberg K, Rossman KL, Der CJ. The Ras superfamily at a glance. J Cell Sci. 2005;118(Pt 5):843-6.

10. Song S, Cong W, Zhou S, Shi Y, Dai W, Zhang H, et al. Small GTPases: Structure, biological function and its interaction with nanoparticles. Asian journal of pharmaceutical sciences. 2019;14(1):30-9.

11. Milburn MV, Tong L, deVos AM, Brunger A, Yamaizumi Z, Nishimura S, et al. Molecular switch for signal transduction: structural differences between active and inactive forms of protooncogenic ras proteins. Science. 1990;247(4945):939-45.

12. Drivas GT, Shih A, Coutavas E, Rush MG, D'Eustachio P. Characterization of four novel ras-like genes expressed in a human teratocarcinoma cell line. Molecular and cellular biology. 1990;10(4):1793-8.

13. Wittinghofer A, Pai EF. The structure of Ras protein: a model for a universal molecular switch. Trends Biochem Sci. 1991;16(10):382-7.

14. Ganotra J, Sharma B, Biswal B, Bhardwaj D, Tuteja N. Emerging role of small GTPases and their interactome in plants to combat abiotic and biotic stress. Protoplasma. 2023;260(4):1007-29.

15. Lu S, Jang H, Muratcioglu S, Gursoy A, Keskin O, Nussinov R, et al. Ras Conformational Ensembles, Allostery, and Signaling. Chem Rev. 2016;116(11):6607-65.

16. Palfy G, Menyhard DK, Perczel A. Dynamically encoded reactivity of Ras enzymes: opening new frontiers for drug discovery. Cancer Metastasis Rev. 2020;39(4):1075-89.

17. Kanade M, Chakraborty S, Shelke SS, Gayathri P. A Distinct Motif in a Prokaryotic Small Ras-Like GTPase Highlights Unifying Features of Walker B Motifs in P-Loop NTPases. J Mol Biol. 2020;432(20):5544-64.

18. Scheffzek K, Ahmadian MR, Wittinghofer A. GTPase-activating proteins: helping hands to complement an active site. Trends Biochem Sci. 1998;23(7):257-62.

19. Wittinghofer F. Caught in the act of the switch-on. Nature. 1998;394(6691):317-9.

20. Cherfils J, Zeghouf M. Regulation of small GTPases by GEFs, GAPs, and GDIs. Physiol Rev. 2013;93(1):269-309.

21. Bischoff FR, Krebber H, Kempf T, Hermes I, Ponstingl H. Human RanGTPase-activating protein RanGAP1 is a homologue of yeast Rna1p involved in mRNA processing and transport. Proc Natl Acad Sci U S A. 1995;92(5):1749-53.

22. Mishra AK, Lambright DG. Invited review: Small GTPases and their GAPs. Biopolymers. 2016;105(8):431-48.

23. van Dam TJ, Bos JL, Snel B. Evolution of the Ras-like small GTPases and their regulators. Small GTPases. 2011;2(1):4-16.

24. Bernards A, Settleman J. GAP control: regulating the regulators of small GTPases. Trends Cell Biol. 2004;14(7):377-85.

25. Scheffzek K, Ahmadian MR. GTPase activating proteins: structural and functional insights 18 years after discovery. Cell Mol Life Sci. 2005;62(24):3014-38.

26. Goitre L, Trapani E, Trabalzini L, Retta SF. The Ras superfamily of small GTPases: the unlocked secrets. Methods in molecular biology (Clifton, NJ). 2014;1120:1-18.

27. Yin G, Huang J, Petela J, Jiang H, Zhang Y, Gong S, et al. Targeting small GTPases: emerging grasps on previously untamable targets, pioneered by KRAS. Signal Transduct Target Ther. 2023;8(1):212.

28. Gorlich D. Transport into and out of the cell nucleus. EMBO J. 1998;17(10):2721-7.

29. Gorlich D, Kutay U. Transport between the cell nucleus and the cytoplasm. Annu Rev Cell Dev Biol. 1999;15:607-60.

30. Pennisi E. The nucleus's revolving door. Science. 1998;279(5354):1129-31.

31. Paci G, Caria J, Lemke EA. Cargo transport through the nuclear pore complex at a glance. J Cell Sci. 2021;134(2).

32. Bley CJ, Nie S, Mobbs GW, Petrovic S, Gres AT, Liu X, et al. Architecture of the cytoplasmic face of the nuclear pore. Science. 2022;376(6598):eabm9129.

33. Aksu M, Trakhanov S, Vera Rodriguez A, Gorlich D. Structural basis for the nuclear import and export functions of the biportin Pdr6/Kap122. J Cell Biol. 2019;218(6):1839-52.

34. Yamazawa R, Jiko C, Choi S, Park IY, Nakagawa A, Yamashita E, et al. Structural Basis for Selective Binding of Export Cargoes by Exportin-5. Structure. 2018;26(10):1393-8 e2.

35. Chook YM, Blobel G. Structure of the nuclear transport complex karyopherin-beta2-Ran x GppNHp. Nature. 1999;399(6733):230-7.

36. Yudin D, Fainzilber M. Ran on tracks - cytoplasmic roles for a nuclear regulator. Journal of Cell Science. 2009;122(5):587-93.

37. Matsuura Y. Mechanistic Insights from Structural Analyses of Ran-GTPase-Driven Nuclear Export of Proteins and RNAs. Journal of Molecular Biology. 2016;428(10):2025-39.

38. Gorlich D, Pante N, Kutay U, Aebi U, Bischoff FR. Identification of different roles for RanGDP and RanGTP in nuclear protein import. EMBO J. 1996;15(20):5584-94.

39. Melchior F, Gerace L. Two-way trafficking with Ran. Trends Cell Biol. 1998;8(5):175-9.

40. Smith A, Brownawell A, Macara IG. Nuclear import of Ran is mediated by the transport factor NTF2. Curr Biol. 1998;8(25):1403-6.

41. Stewart M, Kent HM, McCoy AJ. Structural basis for molecular recognition between nuclear transport factor 2 (NTF2) and the GDP-bound form of the Ras-family GTPase Ran. Journal of Molecular Biology. 1998;277(3):635-46.

42. Stewart M, Kent HM, McCoy AJ. The structure of the Q69L mutant of GDP-Ran shows a major conformational change in the switch II loop that accounts for its failure to bind nuclear transport factor 2 (NTF2). Journal of Molecular Biology. 1998;284(5):1517-27.

43. Ohtsubo M, Okazaki H, Nishimoto T. The RCC1 protein, a regulator for the onset of chromosome condensation locates in the nucleus and binds to DNA. J Cell Biol. 1989;109(4 Pt 1):1389-97.

44. Seki T, Hayashi N, Nishimoto T. RCC1 in the Ran pathway. J Biochem. 1996;120(2):207-14.

45. Renault L, Kuhlmann J, Henkel A, Wittinghofer A. Structural basis for guanine nucleotide exchange on Ran by the regulator of chromosome condensation (RCC1). Cell. 2001;105(2):245-55.

46. Baytshtok V, DiMattia MA, Lima CD. Structural basis for a nucleoporin exportin complex between RanBP2, SUMO1-RanGAP1, the E2 Ubc9, Crm1 and the Ran GTPase. Nat Commun. 2025;16(1):6403.

47. Kalab P, Weis K, Heald R. Visualization of a Ran-GTP gradient in interphase and mitotic

egg extracts. Science. 2002;295(5564):2452-6.

48. Seewald MJ, Korner C, Wittinghofer A, Vetter IR. RanGAP mediates GTP hydrolysis without an arginine finger. Nature. 2002;415(6872):662-6.

49. Takeda E, Hieda M, Katahira J, Yoneda Y. Phosphorylation of RanGAP1 stabilizes its interaction with ran and RanBP1. Cell Struct Funct. 2005;30(1-2):69-80.

50. Moroianu J, Blobel G, Radu A. Nuclear protein import: Ran-GTP dissociates the karyopherin alpha beta heterodimer by displacing alpha from an overlapping binding site on beta. P Natl Acad Sci USA. 1996;93(14):7059-62.

51. Forwood JK, Lonhienne TG, Marfori M, Robin G, Meng W, Guncar G, et al. Kap95p binding induces the switch loops of RanGDP to adopt the GTP-bound conformation: implications for nuclear import complex assembly dynamics. J Mol Biol. 2008;383(4):772-82.

52. Port SA, Monecke T, Dickmanns A, Spillner C, Hofele R, Urlaub H, et al. Structural and Functional Characterization of CRM1-Nup214 Interactions Reveals Multiple FG-Binding Sites Involved in Nuclear Export. Cell Rep. 2015;13(4):690-702.

53. Sun Q, Carrasco YP, Hu Y, Guo X, Mirzaei H, Macmillan J, et al. Nuclear export inhibition through covalent conjugation and hydrolysis of Leptomycin B by CRM1. Proc Natl Acad Sci U S A. 2013;110(4):1303-8.

54. Bischoff FR, Gorlich D. RanBP1 is crucial for the release of RanGTP from importin beta-related nuclear transport factors. FEBS Lett. 1997;419(2-3):249-54.

55. Askjaer P, Jensen TH, Nilsson J, Englmeier L, Kjems J. The specificity of the CRM1-Rev nuclear export signal interaction is mediated by RanGTP. J Biol Chem. 1998;273(50):33414-22.

56. Doherty KJ, McKay C, Chan KK, El-Tanani MK. RAN GTPase as a Target for Cancer Therapy: Ran Binding Proteins. Curr Mol Med. 2011;11(8):686-95.

57. Okada N, Sato M. Spatiotemporal Regulation of Nuclear Transport Machinery and Microtubule Organization. Cells-Basel. 2015;4(3):406-26.

58. Abe H, Kamai T, Shirataki H, Oyama T, Arai K, Yoshida KI. High expression of Ran GTPase is associated with local invasion and metastasis of human clear cell renal cell carcinoma. International Journal of Cancer. 2008;122(10):2391-7.

59. Deng L, Lu YY, Zhao XD, Sun Y, Shi YQ, Fan HW, et al. Ran GTPase protein promotes human pancreatic cancer proliferation by deregulating the expression of Survivin and cell cycle proteins. Biochem Bioph Res Co. 2013;440(2):322-9.

60. Yuen HF, Chan KK, Platt-Higgins A, Dakir el H, Matchett KB, Haggag YA, et al. Ran GTPase promotes cancer progression via Met recepto-rmediated downstream signaling. Oncotarget. 2016;7(46):75854-64.

61. Sazer S, Nurse P. A fission yeast RCC1-related protein is required for the mitosis to interphase transition. The EMBO Journal. 1994;13(3):606-15.

62. Rensen WM, Mangiacasale R, Ciciarello M, Lavia P. The GTPase Ran: regulation of cell life and potential roles in cell transformation. Front Biosci-Landmrk. 2008;13:4097-121.

63. Sazer S, Dasso M. The ran decathlon: multiple roles of Ran. J Cell Sci. 2000;113 (Pt 7):1111-8.

64. Dasso M, Seki T, Azuma Y, Ohba T, Nishimoto T. A mutant form of the Ran/TC4 protein disrupts nuclear function in Xenopus laevis egg extracts by inhibiting the RCC1 protein, a regulator of chromosome condensation. EMBO J. 1994;13(23):5732-44.

65. Kahana JA, Cleveland DW. Beyond nuclear transport. Ran-GTP as a determinant of spindle assembly. J Cell Biol. 1999;146(6):1205-10.

66. Zhang C, Goldberg MW, Moore WJ, Allen TD, Clarke PR. Concentration of Ran on chromatin induces decondensation, nuclear envelope formation and nuclear pore complex assembly. Eur J Cell Biol. 2002;81(11):623-33.

67. Scheffzek K, Klebe C, Fritz-Wolf K, Kabsch W, Wittinghofer A. Crystal structure of the nuclear Ras-related protein Ran in its GDP-bound form. Nature. 1995;374(6520):378-81.

68. Kjeldgaard M, Nyborg J, Clark BF. The GTP binding motif: variations on a theme. FASEB J. 1996;10(12):1347-68.

69. Czigleczki J, de Resende Lara PT, Dudas B, Jang H, Perahia D, Nussinov R, et al. Small GTPase Ran: Depicting the nucleotide-specific conformational landscape of the functionally important C-terminus. Front Mol Biosci. 2023;10:1111574.

70. Nilsson J, Weis K, Kjems J. The C-terminal extension of the small GTPase Ran is essential for defining the GDP-bound form. Journal of Molecular Biology. 2002;318(2):583-93.

71. Richards SA, Lounsbury KM, Macara IG. The C-Terminus of the Nuclear Ran/Tc4 Gtpase Stabilizes the Gdp-Bound State and Mediates Interactions with Rcc1, Ran-Gap, and Htf9a/Ranbp1. Journal of Biological Chemistry. 1995;270(24):14405-11.

72. Vetter IR, Arndt A, Kutay U, Gorlich D, Wittinghofer A. Structural view of the Ran-Importin beta interaction at 2.3 A resolution. Cell. 1999;97(5):635-46.

73. Vetter IR, Nowak C, Nishimoto T, Kuhlmann J, Wittinghofer A. Structure of a Ran-binding domain complexed with Ran bound to a GTP analogue: implications for nuclear transport. Nature. 1999;398(6722):39-46.

74. Nilsson J, Askjaer P, Kjems J. A role for the basic patch and the C terminus of RanGTP in regulating the dynamic interactions with importin β, CRM1 and RanBP1. Journal of Molecular Biology. 2001;305(2):231-43.

75. Güttler T, Görlich D. Ran-dependent nuclear export mediators: a structural perspective. Embo Journal. 2011;30(17):3457-74.

76. Bischoff FR, Krebber H, Smirnova E, Dong WH, Ponstingl H. Coactivation of Rangtpase and Inhibition of Gtp Dissociation by Ran Gtp-Binding Protein Ranbp1. Embo Journal. 1995;14(4):705-15.

77. Seewald MJ, Kraemer A, Farkasovsky M, Körner C, Wittinghofer A, Vetter IR. Biochemical characterization of the Ran-RanBP1-RanGAP system: Are RanBP proteins and the acidic tail of RanGAP required for the Ran-RanGAP GTPase reaction? Molecular and cellular biology. 2003;23(22):8124-36.

78. Guttler T, Madl T, Neumann P, Deichsel D, Corsini L, Monecke T, et al. NES consensus redefined by structures of PKI-type and Rev-type nuclear export signals bound to CRM1. Nat Struct Mol Biol. 2010;17(11):1367-76.

79. Monecke T, Guttler T, Neumann P, Dickmanns A, Gorlich D, Ficner R. Crystal structure of the nuclear export receptor CRM1 in complex with Snurportin1 and RanGTP. Science. 2009;324(5930):1087-91.

80. Koyama M, Matsuura Y. An allosteric mechanism to displace nuclear export cargo from CRM1 and RanGTP by RanBP1. EMBO J. 2010;29(12):2002-13.

81. Grunwald M, Lazzaretti D, Bono F. Structural basis for the nuclear export activity of Importin13. EMBO J. 2013;32(6):899-913.

82. Petrenko R, Meller J. Molecular Dynamics. Encyclopedia of Life Sciences.

83. Sagui C, Darden TA. Molecular dynamics simulations of biomolecules: long-range electrostatic effects. Annu Rev Biophys Biomol Struct. 1999;28:155-79.

84. Hug S. Classical molecular dynamics in a nutshell. Methods in molecular biology (Clifton, NJ). 2013;924:127-52.

85. Banavali NK, Roux B. Free Energy Landscape of A-DNA to B-DNA Conversion in Aqueous Solution. Journal of the American Chemical Society. 2005;127(18):6866-76.

86. Terakawa T, Takada S. p53 dynamics upon response element recognition explored by molecular simulations. Scientific Reports. 2015;5(1):17107.

87. Allen MP, Tildesley DJ. Computer Simulation of Liquids: Oxford University Press; 2017 23 Nov 2017.

88. Dodson GG, Lane DP, Verma CS. Molecular simulations of protein dynamics: new windows on mechanisms in biology. EMBO reports. 2008;9(2):144-50.

89. Karplus M, Kuriyan J. Molecular dynamics and protein function. Proc Natl Acad Sci U S A. 2005;102(19):6679-85.

90. Leach AR. Molecular modelling : principles and applications. 2nd ed. Harlow, England ; New York: Prentice Hall; 2001. xxiv, 744 p., 16 p. of plates p.

91. Bashford D, Case DA. Generalized Born Models of Macromolecular Solvation Effects. 2000;51(Volume 51, 2000):129-52.

92. Kukol A. Molecular modeling of proteins. Totowa, NJ: Humana Press; 2008. xi, 390 p. p.

93. Verlet L. Computer "Experiments" on Classical Fluids. I. Thermodynamical Properties of Lennard-Jones Molecules. Physical Review. 1967;159(1):98-103.

94. Swope WC, Andersen HC, Berens PH, Wilson KR. A computer simulation method for the calculation of equilibrium constants for the formation of physical clusters of molecules: Application to small water clusters. The Journal of Chemical Physics. 1982;76(1):637-49.

95. Hockney RW, Goel SP, Eastwood JW. Quiet high-resolution computer models of a plasma. Journal of Computational Physics. 1974;14(2):148-58.

96. Costa MGS, Batista PR, Bisch PM, Perahia D. Exploring Free Energy Landscapes of Large Conformational Changes: Molecular Dynamics with Excited Normal Modes. Journal of Chemical Theory and Computation. 2015;11(6):2755-67.

97. Ghysels A, Van Speybroeck V, Pauwels E, Catak S, Brooks BR, Van Neck D, et al. Comparative study of various normal mode analysis techniques based on partial Hessians. 2010;31(5):994-1007.

98. Batista PR, Robert CH, Marechal JD, Hamida-Rebai MB, Pascutti PG, Bisch PM, et al. Consensus modes, a robust description of protein collective motions from multiple-minima normal mode analysis--application to the HIV-1 protease. Phys Chem Chem Phys. 2010;12(12):2850-9.

99. Floquet N, Marechal JD, Badet-Denisot MA, Robert CH, Dauchez M, Perahia D. Normal mode analysis as a prerequisite for drug design: application to matrix metalloproteinases inhibitors. FEBS Lett. 2006;580(22):5130-6.

100. Hayward S, de Groot BL. Normal modes and essential dynamics. Methods in molecular biology (Clifton, NJ). 2008;443:89-106.

101. Resende-Lara PT, Costa MGS, Dudas B, Perahia D. Adaptive collective motions: a hybrid method to improve conformational sampling with molecular dynamics and normal modes. 2022:2022.11.29.517349.

102. Berman HM, Westbrook J, Feng Z, Gilliland G, Bhat TN, Weissig H, et al. The Protein Data Bank. Nucleic Acids Research. 2000;28(1):235-42.

103. Rudack T, Jenrich S, Brucker S, Vetter IR, Gerwert K, Kotting C. Catalysis of GTP hydrolysis by small GTPases at atomic detail by integration of X-ray crystallography, experimental, and theoretical IR spectroscopy. J Biol Chem. 2015;290(40):24079-90.

104. Sondergaard CR, Olsson MH, Rostkowski M, Jensen JH. Improved Treatment of Ligands and Coupling Effects in Empirical Calculation and Rationalization of pKa Values. J Chem Theory Comput. 2011;7(7):2284-95.

105. Brooks BR, Brooks CL, 3rd, Mackerell AD, Jr., Nilsson L, Petrella RJ, Roux B, et al. CHARMM: the biomolecular simulation program. J Comput Chem. 2009;30(10):1545-614.

106. Jo S, Cheng X, Islam SM, Huang L, Rui H, Zhu A, et al. CHARMM-GUI PDB manipulator for advanced modeling and simulations of proteins containing nonstandard residues. Adv Protein Chem Struct Biol. 2014;96:235-65.

107. Jo S, Kim T, Iyer VG, Im W. CHARMM-GUI: a web-based graphical user interface for CHARMM. J Comput Chem. 2008;29(11):1859-65.

108. Lee J, Cheng X, Swails JM, Yeom MS, Eastman PK, Lemkul JA, et al. CHARMM-GUI Input Generator for NAMD, GROMACS, AMBER, OpenMM, and CHARMM/OpenMM Simulations Using the CHARMM36 Additive Force Field. Journal of Chemical Theory and Computation. 2016;12(1):405-13.

109. Darden T, York D, Pedersen L. Particle mesh Ewald: An N·log(N) method for Ewald sums in large systems. The Journal of Chemical Physics. 1993;98(12):10089-92.

110. Snyman JA, Wilke DN. Practical Mathematical Optimization: Basic Optimization Theory and Gradient-Based Algorithms: Springer International Publishing; 2018.

111. Ben-Israel A. A Newton-Raphson method for the solution of systems of equations. Journal of Mathematical Analysis and Applications. 1966;15(2):243-52.

112. Brooks BR, Bruccoleri RE, Olafson BD, States DJ, Swaminathan S, Karplus M. CHARMM: A program for macromolecular energy, minimization, and dynamics calculations. 1983;4(2):187-217.

113. Best RB, Zhu X, Shim J, Lopes PE, Mittal J, Feig M, et al. Optimization of the additive CHARMM all-atom protein force field targeting improved sampling of the backbone phi, psi and side-chain chi(1) and chi(2) dihedral angles. J Chem Theory Comput. 2012;8(9):3257-73.

114. Huang J, MacKerell AD, Jr. CHARMM36 all-atom additive protein force field: validation based on comparison to NMR data. J Comput Chem. 2013;34(25):2135-45.

115. Czigleczki J, Dudas B, Balog E. Induced opening of conformational switch I in GTP-bound Ran GTPase. Protein Science. 2026;35(3):e70478.

116. Heyer LJ, Kruglyak S, Yooseph SJGr. Exploring expression data: identification and analysis of coexpressed genes. 1999;9 11:1106-15.

117. Dudas B, Merzel F, Jang H, Nussinov R, Perahia D, Balog E. Nucleotide-Specific Autoinhibition of Full-Length K-Ras4B Identified by Extensive Conformational Sampling. Front Mol Biosci. 2020;7:145.

118. Bacot-Davis VR, Palmenberg AC. NMR solution structure of nucleotide-free Ran GTPase. Worldwide Protein Data Bank2016.

119. Schrader N, Koerner C, Koessmeier K, Bangert JA, Wittinghofer A, Stoll R, et al. The crystal structure of the Ran-Nup153ZnF2 complex: a general Ran docking site at the nuclear pore complex. Structure. 2008;16(7):1116-25.

120. Partridge JR, Schwartz TU. Crystallographic and biochemical analysis of the Ran-binding zinc finger domain. J Mol Biol. 2009;391(2):375-89.

121. Etchin J, Sun Q, Kentsis A, Farmer A, Zhang ZC, Sanda T, et al. Antileukemic activity of nuclear export inhibitors that spare normal hematopoietic cells. Leukemia. 2013;27(1):66-74.

122. Haines JD, Herbin O, de la Hera B, Vidaurre OG, Moy GA, Sun Q, et al. Nuclear export inhibitors avert progression in preclinical models of inflammatory demyelination. Nat Neurosci. 2015;18(4):511-20.

123. Fung HY, Fu SC, Brautigam CA, Chook YM. Structural determinants of nuclear export signal orientation in binding to exportin CRM1. Elife. 2015;4.

124. Fung HY, Fu SC, Chook YM. Nuclear export receptor CRM1 recognizes diverse conformations in nuclear export signals. Elife. 2017;6.

125. Lei Y, An Q, Shen XF, Sui M, Li C, Jia D, et al. Structure-Guided Design of the First Noncovalent Small-Molecule Inhibitor of CRM1. J Med Chem. 2021;64(10):6596-607.

126. Baumhardt JM, Walker JS, Lee Y, Shakya B, Brautigam CA, Lapalombella R, et al. Recognition of nuclear export signals by CRM1 carrying the oncogenic E571K mutation. Mol Biol Cell. 2020;31(17):1879-91.

127. Walker JS, Hing ZA, Harrington B, Baumhardt J, Ozer HG, Lehman A, et al. Recurrent XPO1 mutations alter pathogenesis of chronic lymphocytic leukemia. J Hematol Oncol. 2021;14(1):17.

128. Murphy GA, Moore MS, Drivas G, delaOssa PP, Villamarin A, DEustachio P, et al. A T42A Ran mutation: Differential interactions with effectors and regulators, and defect in nuclear protein import. Mol Biol Cell. 1997;8(12):2591-604.

129. Baussand J, Kleinjung J. Specific Conformational States of Ras GTPase upon Effector Binding. Journal of Chemical Theory and Computation. 2013;9(1):738-49.

130. Calixto AR, Moreira C, Pabis A, Kotting C, Gerwert K, Rudack T, et al. GTP Hydrolysis Without an Active Site Base: A Unifying Mechanism for Ras and Related GTPases. J Am Chem Soc. 2019;141(27):10684-701.

131. Dudas B, Perahia D, Balog E. Revealing the activation mechanism of autoinhibited RalF by integrated simulation and experimental approaches. Scientific Reports. 2021;11(1):10059.

132. Gorfe AA, Grant BJ, McCammon JA. Mapping the nucleotide and isoform-dependent structural and dynamical features of ras proteins. Structure. 2008;16(6):885-96.

133. Kumawat A, Chakrabarty S, Kulkarni K. Nucleotide Dependent Switching in Rho GTPase: Conformational Heterogeneity and Competing Molecular Interactions. Sci Rep. 2017;7:45829.

134. Gauto DF, Macek P, Barducci A, Fraga H, Hessel A, Terauchi T, et al. Aromatic Ring Dynamics, Thermal Activation, and Transient Conformations of a 468 kDa Enzyme by Specific (1)H-(13)C Labeling and Fast Magic-Angle Spinning NMR. J Am Chem Soc. 2019;141(28):11183-95.

135. Dreydoppel M, Raum HN, Weininger U. Slow ring flips in aromatic cluster of GB1 studied by aromatic (13)C relaxation dispersion methods. J Biomol NMR. 2020;74(2-3):183-91.

136. Akke M, Weininger U. NMR Studies of Aromatic Ring Flips to Probe Conformational Fluctuations in Proteins. J Phys Chem B. 2023;127(3):591-9.

137. Wolf FI, Cittadini A. Chemistry and biochemistry of magnesium. Mol Aspects Med. 2003;24(1-3):3-9.

138. Ly TK, Wang JB, Pereira R, Rojas KS, Peng X, Feng QY, et al. Activation of the Ran GTPase Is Subject to Growth Factor Regulation and Can Give Rise to Cellular Transformation. Journal of Biological Chemistry. 2010;285(8):5815-26.

139. Milano SK, Kwon W, Pereira R, Antonyak MA, Cerione RA. Characterization of a Novel Activated Ran GTPase Mutant and Its Ability to Induce Cellular Transformation. Journal of Biological Chemistry. 2012;287(30):24955-66.

140. Rösch P, Wittinghofer A, Tucker J, Sczakiel G, Leberman R, Schlichting I. 31P-NMR spectra of the Ha-ras p21. Nucleotide complexes. Biochem Bioph Res Co. 1986;135(2):549-55.

141. Pai EF, Kabsch W, Krengel U, Holmes KC, John J, Wittinghofer A. Structure of the guanine-nucleotide-binding domain of the Ha-ras oncogene product p21 in the triphosphate conformation. Nature. 1989;341(6239):209-14.

142. Spoerner M, Herrmann C, Vetter IR, Kalbitzer HR, Wittinghofer A. Dynamic properties of the Ras switch I region and its importance for binding to effectors. Proc Natl Acad Sci U S A. 2001;98(9):4944-9.

143. Araki M, Shima F, Yoshikawa Y, Muraoka S, Ijiri Y, Nagahara Y, et al. Solution structure of the state 1 conformer of GTP-bound H-Ras protein and distinct dynamic properties between the state 1 and state 2 conformers. J Biol Chem. 2011;286(45):39644-53.

144. Boriack-Sjodin PA, Margarit SM, Bar-Sagi D, Kuriyan J. The structural basis of the activation of Ras by Sos. Nature. 1998;394(6691):337-43.

145. Margarit SM, Sondermann H, Hall BE, Nagar B, Hoelz A, Pirruccello M, et al. Structural Evidence for Feedback Activation by Ras·GTP of the Ras-Specific Nucleotide Exchange Factor SOS. Cell. 2003;112(5):685-95.

146. Van Holsbeeck K, Fischer B, Gonzalez S, Gadais C, Versees W, Martins JC, et al. Nanobody Loop Mimetics Enhance Son of Sevenless 1-Catalyzed Nucleotide Exchange on RAS. Angew Chem Int Ed Engl. 2023;62(24):e202219095.

147. Geyer M, Schweins T, Herrmann C, Prisner T, Wittinghofer A, Kalbitzer HR. Conformational transitions in p21ras and in its complexes with the effector protein Raf-RBD and the GTPase activating protein GAP. Biochemistry. 1996;35(32):10308-20.

148. Kalbitzer HR, Spoerner M, Ganser P, Hozsa C, Kremer W. Fundamental link between folding states and functional states of proteins. J Am Chem Soc. 2009;131(46):16714-9.

149. Matsumoto S, Miyano N, Baba S, Liao J, Kawamura T, Tsuda C, et al. Molecular Mechanism for Conformational Dynamics of Ras.GTP Elucidated from In-Situ Structural Transition in Crystal. Sci Rep. 2016;6:25931.

150. Miyakawa T, Morikawa R, Takasu M, Sugimori K, Kawaguchi K, Saito H, et al. A molecular dynamics study of Hras-GTP and GDP complexes: The properties of water molecules around guanine nucleotide. AIP Conference Proceedings. 2013;1518(1):594-7.

151. Mori K, Hata M, Neya S, Hoshino T. A study on the role of Mg2+ in a Ras protein by MD simulation. Chem-bio Informatics Journal. 2002;2:147-55.

152. Palfy G, Menyhard DK, Akontz-Kiss H, Vida I, Batta G, Toke O, et al. The Importance of Mg(2+) -Free State in Nucleotide Exchange of Oncogenic K-Ras Mutants. Chemistry. 2022;28(59):e202201449.

153. Xiong Y, Zeng J, Xia F, Cui Q, Deng X, Xu X. Conformations and binding pockets of HRas and its guanine nucleotide exchange factors complexes in the guanosine triphosphate exchange process. J Comput Chem. 2022;43(13):906-16.

154. Tammsalu T, Matic I, Jaffray EG, Ibrahim AFM, Tatham MH, Hay RT. Proteome-wide identification of SUMO2 modification sites. Science signaling. 2014;7(323):rs2.

155. Sakin V, Richter SM, Hsiao HH, Urlaub H, Melchior F. Sumoylation of the GTPase Ran by the RanBP2 SUMO E3 Ligase Complex. J Biol Chem. 2015;290(39):23589-602.

9. BIBLIOGRAPHY OF THE CANDIDATE'S PUBLICATIONS

Czigleczki J, de Resende Lara PT, Dudas B, Jang H, Perahia D, Nussinov R, et al. Small GTPase Ran: Depicting the nucleotide-specific conformational landscape of the functionally important C-terminus. Front Mol Biosci. 2023;10:1111574.

Czigleczki J, Dudas B, Balog E. Induced opening of conformational switch I in GTP-bound Ran GTPase. 2026;35(3):e70478.

10. ACKNOWLEDGEMENTS

I would like to begin by expressing my sincere gratitude to my wonderful supervisor, Erika Balog, for her invaluable advice and continuous support throughout my Ph.D. studies. Although this journey has not been without its challenges, she taught me how to focus on my research topic and how to conduct scientific work in a thorough and meticulous manner. Erika, I learned a great deal from you—not only as a scientist, but also as a responsible and thoughtful person. I will always remember the advice and support you gave me, both professionally and personally.

I would also like to thank all my colleagues at the Biophysics Institute. I am grateful to Bálint Dudás for explaining research approaches in an easily understandable way and with such enthusiasm that he made even difficult tasks seem achievable. I would like to thank Dániel Tóth for his expert advice in the complex fields of pharmaceuticals and biochemistry, especially when I needed it the most.

I am thankful to the Biophysics Institute and to Miklós Kellermayer for their support and for providing me with the opportunity to pursue this professional career. It has been an honor to work in such an inspiring environment.

Finally, I would like to thank my family, especially my husband, who has supported me through both the best and the most difficult times, rarely questioning my decision to pursue a career in research rather than immediately pursuing a different professional path outside academia. I have no words to express my gratitude for this incredible support. Thank you so much!